

Title goes here

Bálint Balázs



Pázmány Péter Catholic University
Faculty of Information Technology



European Molecular Biology Laboratory

Supervisors: Lars Hufnagel, Balázs Rózsa

A thesis submitted for the degree of
Doctor of Philosophy
2017

Abstract

Abstract in English.

Tartlami kivonat

Absztrakt magyarul.

Contents

Abstract	iii
Tartlami kivonat	v
List of Figures	x
List of Tables	xi
Introduction	1
1 Light-sheet imaging of mammalian development	3
1.1 Wide-field fluorescence microscopy	5
1.1.1 Fluorescent proteins	6
1.1.2 Wide-field image formation	6
1.1.3 Resolution of a wide-field microscope	8
1.2 Imaging in three dimensions	11
1.2.1 Laser scanning confocal microscopy	12
1.2.2 Confocal-theta microscopy	14
1.3 Light-sheet microscopy	15
1.3.1 Optics of light-sheet microscopy	18
1.3.2 Static light-sheet illumination	18
1.3.3 Digitally scanned light-sheet illumination	20
1.4 Multi-view light-sheet microscopy	22
1.5 Image processing for multi-view microscopy	23
1.5.1 Registration	24
1.5.2 Transformation	24
1.5.3 Image fusion	24
1.6 Image compression	24
1.6.1 Entropy coding	25
1.6.2 Transform coding	30
1.6.3 Differential pulse code modulation / LOCO-I?	34

CONTENTS

2	Dual Mouse-SPIM	35
2.1	Previous Mouse-SPIM	35
2.2	Light collection efficiency of an objective	35
2.3	Optical layout	37
2.4	Optical alignment	37
2.4.1	Alignment of illuminaiton branches	39
2.4.2	Alignment of detection branches	40
2.5	Results	41
2.5.1	Characterizing illumination profile	42
2.5.2	Resolution and point spread function measurement	42
3	Real-time, GPU accelerated image processing pipeline	45
3.1	GPU architecture	45
3.2	Live fusion	45
3.2.1	MuVi-SPIM	45
3.2.2	Bead based registration	45
3.3	B ³ D image compression	45
3.3.1	Data sizes in microscopy	45
3.3.2	Lossless compression performance	45
3.3.3	Benchmarking	45
3.4	Noise dependent lossy compression	45
3.5	Methods	45
4	Discussion	51
4.1	New scientific results	51
	Acknowledgements	53
	Appendix A: Bill of materials	55
	References	57

List of Figures

1.1	Excitation and emission spectrum of enhanced green fluorescent protein (EGFP)	5
1.2	Wide-field fluorescence microscope	7
1.3	Airy pattern	9
1.4	Axial cross section of the PSF and OTF of a wide-field microscope	9
1.5	Resolution of a wide-field microscope	11
1.6	Basic optical components of a laser scanning confocal and confocal-theta microscope	13
1.7	Axial cross section of the PSF and OTF of a laser scanning confocal microscope	14
1.8	Basic concept of single-plane illumination microscopy	15
1.9	Basic optical components of a SPIM	17
1.10	Axial cross section of the PSF and OTF of a single plane illumination microscope	18
1.11	Light-sheet dimensions	21
1.12	DSLM illumination	22
1.13	Different optical arrangements for light-sheet microscopy	23
1.14	Building the binary Huffman tree	27
1.15	Arithmetic coding scheme in practice with the alphabet from Table 1.4 on the sequence a_1, a_2, a_3	29
1.16	Basis functions of the 8×8 2D DCT, computed as the outer product of the 1D basis vectors.	31
1.17	Multi-resolution wavelet decomposition, using the Haar wavelets as an example	33
2.1	Light collection efficiency of an objective	36
2.2	Axial cross section of the PSF and OTF of a multi-view single plane illumination microscope	37
2.3	Simplified schematics for illumination	37

LIST OF FIGURES

2.4	Dual Mouse SPIM optical layout	38
2.5	Front view of the Dual Mouse-SPIM	42
2.6	Illumination beam profile	43
2.7	Simulated and measured PSF of Dual Mouse-SPIM	44
3.1	Experiment sizes and data rate of different imaging modalities.	46
3.2	Lossless compression performance	47
3.3	Lossless compression performance.	49

List of Tables

1.1	Examples of a random binary code (#1) and a prefix-free binary code (#2)	26
1.2	Huffman code table	27
1.3	Huffman code table	28
1.4	Example alphabet for arithmetic coding	29
3.1	Data sizes in microscopy	46
3.2	Lossless compression performance	47
3.3	Datasets used for benchmarking compression performance	48

LIST OF TABLES

Introduction

INTRODUCTION

Chapter 1

Light-sheet imaging of mammalian development

Unraveling the secrets of mammalian development has been a long standing challenge for developmental biologists and medical professionals alike. Understanding early embryonic development allows to shed light on questions such as human infertility and congenital diseases [todo]. This phase of early life is an incredibly complex and dynamic process spanning through large scales in space and time. Subcellular processes at the nanoscale are happening in the range of milliseconds or faster, while whole embryo reorganizations and tissue migration events take place over the course of hours [1]. Resolving these processes presents a true challenge, since to also understand the underlying mechanisms molecular specificity is just as crucial as high spatial and temporal resolution.

Fluorescence microscopy [2]

The most commonly used model organism for these kind of questions is the mouse embryo, that exhibits several common features to human development, and allows to study it. It has several advantages: full genome is sequenced [3], relatively fast reproduction rate facilitating genetic modifications, already extensively developed tools for genetics and handling [4, 5]. All of these make the mouse embryo the primary model organism when investigating biological processes in mammals.

fixed samples, histology, immunofluorescence -> no time lapse

ex vivo embryo culture

Hooke's Micrographia 1665 [6]

Marvin Minsky confocal microscope, no laser, moving sample [7] first laser scanning confocal: sample stationary, objective is moved Davidovits and Egger [8] first application of laser scanning confocal in "observation of endothelial cells lining the inside of the cornea" [9]

Imaging mouse embryonic development is an extremely challenging task, due to the

1. LIGHT-SHEET IMAGING OF MAMMALIAN DEVELOPMENT

intrauterine development of embryos. Although this prevents direct access to the embryos, for some developmental stages it is possible to culture them in an *ex vivo* environment using special media and carefully controlled environmental conditions [10, 11]. A second hurdle, aside from *in vitro* culturing, arises from the extreme light sensitivity [12] of these embryos, hindering the possibility of long term time-lapse experiments in standard confocal microscopes. Even a few hours of imaging every 15 mins can impair or arrest normal development [J1].

Despite these difficulties, numerous studies successfully used confocal microscopy to image live embryos in an *ex vivo* environment, although these studies typically only mostly wide-field, Oct4 - self renewal of pluripotent stem cells in ICM/epiblast [13]

Sox2 in ICM, also maternal proteins important, similar role as Oct4 Both Oct4 and Sox2 are necessary for ICM formation, without cells become trophoectoderm. Furthermore, for extraembryonic endoderm (ExEn) only Oct4 is required, while for extraembryonic ectoderm (ExE) only Sox2 is required. No time lapse, but confocal used to locate proteins in embryo [14]

inactivation of X chromosome and histone macroH2A1 mouse liver in confocal - fixed samples [15]

antibodies against amyloid β -peptide reduce Alzheimer in mouse, cryostat sections of mouse brain imaged in confocal[16]

aorta imaging in embryo slices, confocal, live stem cells from aorta endothelium? [17]

fixed embryos, maintaining pluripotency in embryonic stem cells[18]

imaging thrombus formation in real time with intravital high-speed confocal microscopy[19]

turning blood into brain hematopoietic stem cells migrate to brain and express neuron-specific antigens [20]

papers from Takashi: apical domain for symmetry breaking [21]

Asymmetric division of contractile domains couples cell positioning and fate specification, Jean-Léon + Hervé [22]

specification of first embryonic lineage, venus trap [23]

surface tension and compaction [24]

self organization framework for symmetry breaking (review)

uj regi cikk Keller [25]

Light microscopy is one of the oldest methods that is still widely used today to investigate the inner workings of microscopic life. Light-sheet microscopy is a relatively new addition to the arsenal of tools that comprise light microscopy methods, and is especially suitable for live imaging of embryonic samples over extended periods of time [26, 27]. It is also easily adapted to the sample, allowing to image a large variety of specimens, from entire organs, such as cleared mouse brains [28], to the subcellular

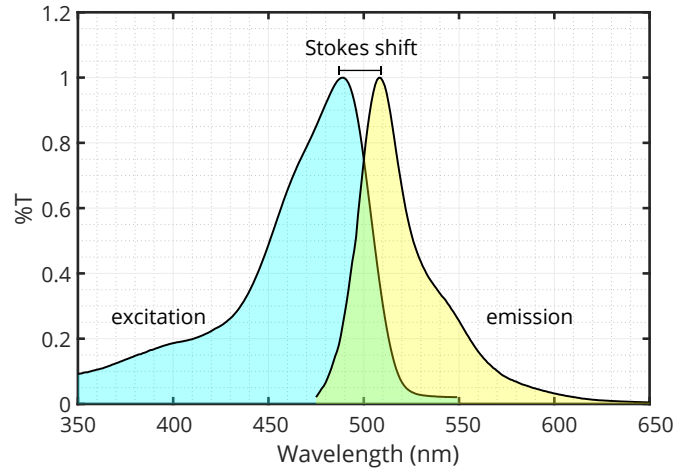


Figure 1.1: Excitation and emission spectrum of enhanced green fluorescent protein (EGFP). Excitation spectrum in blue, emission spectrum in yellow. The separation between the two spectra is due to the Stokes shift, which is 19 nm for EGFP. Data from [31]. Emitted and excitation light can be separated by a long-pass filter at 500 nm.

processes occurring inside cultured cells [29].

1.1 Wide-field fluorescence microscopy

Fluorescence microscopy [30], as a subset of light microscopy is one of the few methods that allow subcellular imaging of live specimens. As the name of the technique suggests, this method collects fluorescent light from the specimens which has numerous advantages, but also some drawbacks. Since biological tissue is usually not fluorescent, except for some autofluorescence at shorter wavelengths, fluorescent dyes or proteins have to be introduced to the system in order to be able to collect the necessary information.

A fluorescent molecule is capable of absorbing photons in a given range (excitation spectrum) and temporarily store its energy by having an electron in a higher energy orbital, *i.e.* in an excited state. This excited state, however is not stable, and the electron quickly jumps back to the ground state while emitting a photon with equal energy to the energy difference between the excited and ground states. The energy of the absorbed and emitted photons are not the same, however. Energy loss occurs due to internal relaxation events, and the emitted photon has lower energy than the excitation photon. This phenomenon is called the Stokes shift, or red shift [**stokes**], and can be exploited in microscopy to drastically increase the signal to noise ratio by filtering out the illumination light (Fig. 1.1).

1. LIGHT-SHEET IMAGING OF MAMMALIAN DEVELOPMENT

1.1.1 Fluorescent proteins

Traditionally synthetic fluorescent dyes were used to label certain structures in the specimens. Some of these directly bind to their target, such as DAPI to DNA, and others can be used when conjugated to an antibody specific to the structure of interest. The drawback of these methods is that the fluorescent label has to be added to the sample from an external source, and in many cases this also necessitates sample preparation techniques incompatible with live imaging, such as fixation [!!!].

The discovery of fluorescent proteins have revolutionized fluorescence microscopy. Since these molecules are proteins, they can be produced directly by the organism if the proper genetic modifications are performed. Even though this was a hurdle at the time of discovering the green fluorescent protein (GFP) [32], the first of its kind, genetic engineering techniques evolved since then [33], and not only has it been successfully integrated in the genome of nematodes [34], zebrafish [35], and mice [36], but many variants have been also engineered by introducing mutations to increase fluorescence intensity, and to change the fluorescent spectrum to allow multicolor imaging [36–39]. The usefulness and impact of these proteins are so profound, that in 2008 the Nobel Prize in chemistry was awarded to Osamu Shimomura, Martin Chalfie, and Roger Tsien “for the discovery and development of the green fluorescent protein, GFP” [40].

1.1.2 Wide-field image formation

By imaging fluorescently labeled specimens, a wide-field fluorescence microscope has the capability of discriminating illumination light from fluorescent light due to the Stokes shift described in the previous section. The microscope’s operating principle is depicted in Figure 1.2.

A light source, typically a mercury lamp is focused on the back focal plane of the objective to create even illumination at the sample. Before entering the objective, the light is filtered, so only those wavelengths that correspond to the excitation properties of the observed fluorophores are transmitted. Since the same objective is used for both illumination and detection, a dichroic mirror is utilized to decouple the illumination and detection paths. The emitted light is filtered again to make sure any reflected and scattered light from the illumination source is blocked to increase signal to noise ratio.

Finally, the light is focused by a tube lens to create a magnified image in the camera sensor. This type of imaging is called infinity corrected optics, since the back focal point of the objective is in “infinity”, meaning that the light exiting the back aperture is parallel. This is achieved by placing the sample exactly at the focal point of the objective. Infinity corrected optics has the advantage that it allows placing various additional optical elements in the infinity space (*i.e.* the space between the objective and the tube lens) without affecting the image quality. In this example such elements are the dichroic

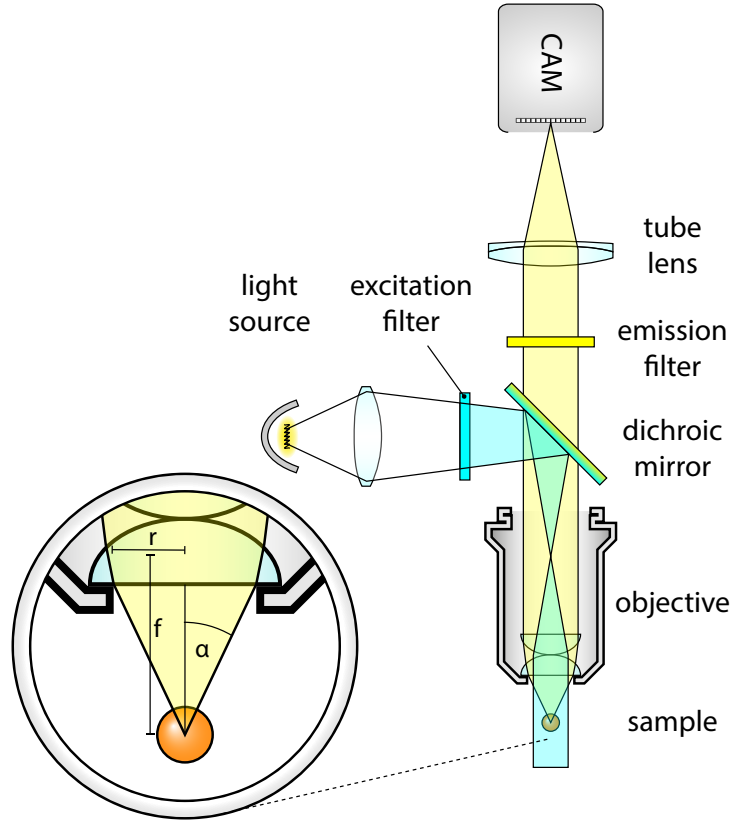


Figure 1.2: Wide-field fluorescence microscope. (a) The light source is focused on the back focal plane of the objective to provide an even illumination to the sample. Emitted photons are collected by the objective, and are separated from the illumination light by a dichroic mirror. (b) , α

mirror and the emission filter.

The combination of the objective and tube lens together will determine the magnification of the system, it will be the ratio of the focal lengths of these lenses:

$$M = \frac{f_{TL}}{f_{OBJ}}. \quad (1.1)$$

The final field of view of the microscope will depend on the magnification, and also on the size of the imaging sensor:

$$FOV = \frac{A}{M}, \quad (1.2)$$

where A is the area of the sensor.

Apart from magnification, the most important property of the objective is the half-angle of the light acceptance cone, α . This not only determines the amount of collected light, but also the achievable resolution of the system (see next section). This angle depends on the size of the lens relative to its focal length. In other words depends on the aperture of the lens, which is why the expression numerical aperture is more commonly

1. LIGHT-SHEET IMAGING OF MAMMALIAN DEVELOPMENT

used to express this property of the objective:

$$NA = n \cdot \sin \alpha. \quad (1.3)$$

For small α angles, the following approximation holds true: $\sin \alpha \approx \tan \alpha \approx \alpha$. Thus, the numerical aperture can also be expressed as a ratio of the radius of the lens and the focal length:

$$NA \approx n \frac{r}{f}, \quad \text{when } \alpha \ll 1. \quad (1.4)$$

1.1.3 Resolution of a wide-field microscope

The resolution of an optical systems is defined by the size of the smallest distinguishable feature on the image. Practically this means the minimum distance between two point like objects so that the two objects can still be resolved. This mainly depends on two factors: the NA of the objective, and the pixel size of the imaging sensor.

Even if the imaging sensor would have infinitely fine resolution, it is not possible to reach arbitrary high resolutions due to the wave nature of light and diffraction effects that occur at the aperture of the objective. This means that depending on the wavelength of the light, any point source will have a finite size on the image that will limit the resolution. The shape of this image is called the *point spread function*, or PSF, as this function describes the behavior of the optical system when imaging a point like source. This property of lenses was already discovered by Abbe in 1873 [41], when he constructed his famous formula for resolution:

$$\delta = \frac{\lambda}{2 \cdot NA}. \quad (1.5)$$

where d is the smallest distance between two distinguishable features.

This equation can be also derived from the scalar theory of diffraction using a paraxial approximation (Fraunhofer diffraction, [42]) that describes the intensity of the electric field in the focus of a lens [43]:

$$H(u, v) = C_0 \left| \int_0^1 J_0(vr) e^{-i\frac{1}{2}ur^2} r dr \right|^2, \quad (1.6)$$

where C_0 is a normalization constant, and J_0 is the zero order Bessel function of the first kind. Furthermore, instead of the commonly used Cartesian coordinates x , y and z , the following optical coordinates are defined:

$$v = \frac{2\pi nr}{\lambda_0} \sin \alpha, \quad u = \frac{8\pi nz}{\lambda_0} \sin^2 \frac{\alpha}{2} \quad (1.7)$$

where $r = \sqrt{x^2 + y^2}$ is the distance from the optical axis, and α is the light collection

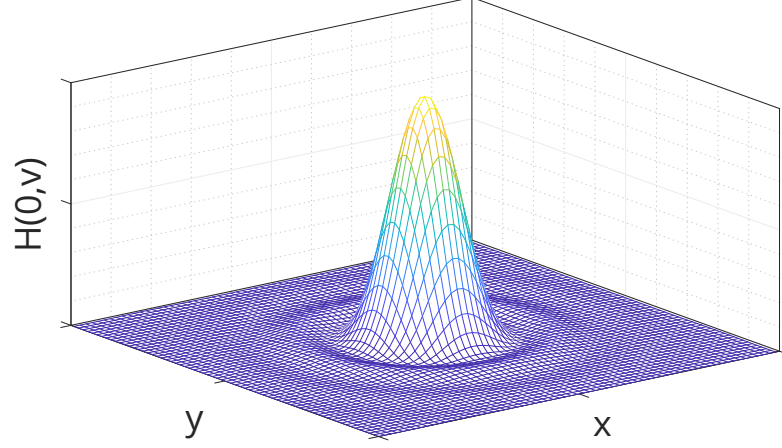


Figure 1.3: Airy pattern. Airy pattern calculated in Matlab based on Eq. (1.8)

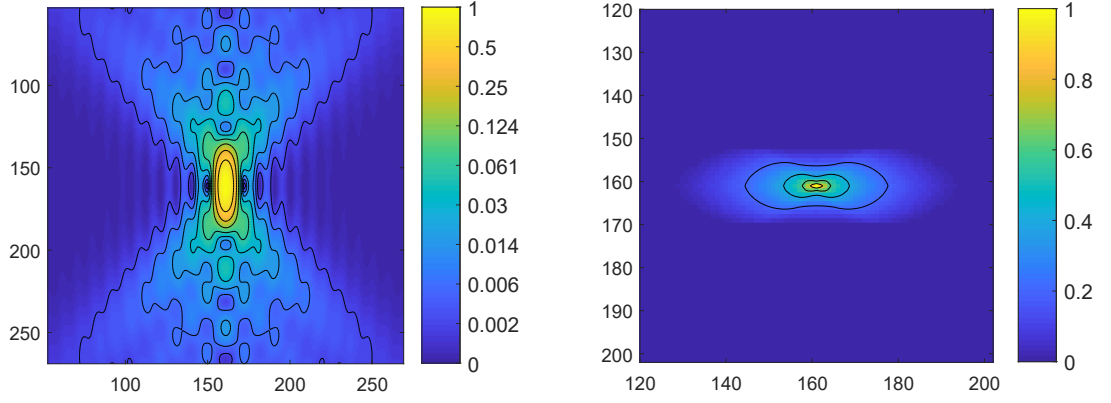


Figure 1.4: Axial cross section of the PSF and OTF of a wide-field microscope. Simulated PSF and OTF for a wide-field microscope with a water immersion objective ($n = 1.33$). $NA = 1.1$, $\lambda = 510$ nm

angle as shown on Fig. 1.2.

To determine the lateral resolution of the system, let's substitute $u = 0$ as the axial optical coordinate, and evaluate Eq. (1.6) which will give the intensity distribution in the focal plane:

$$H(0, v) = C_0 \left| \int_0^1 J_0(vr) r dr \right|^2 = \left(2 \frac{J_1(v)}{v} \right)^2, \quad (1.8)$$

where J_1 is the first order Bessel function of the first kind. This equation describes the famous Airy pattern (Fig. 1.3) which will be the shape of the PSF in the focal plane. The width of this pattern is the resolution, and although there are multiple definitions for this, the most commonly accepted is the Rayleigh criterion [rayleigh] which defines

1. LIGHT-SHEET IMAGING OF MAMMALIAN DEVELOPMENT

the resolution as the distance between the central peak and the first local minimum. As this lies at $v = 3.38$, the resolution can be expressed by substituting this value to Eq. (1.7) and calculating the real distance (r):

$$\delta_{xy} = \frac{3.83}{2\pi} \frac{\lambda_0}{n \cdot \sin \alpha} \approx 0.61 \frac{\lambda_0}{NA}, \quad (1.9)$$

which is equivalent to Abbe's original formula (Eq. (1.5)). The only difference is the scaling factor which is due to the slightly different interpretations of width of the Airy disk as mentioned earlier.

Similarly, to calculate the intensity distribution along the axial axis, let's substitute $v = 0$ to Eq. (1.6):

$$H(u, 0) = C_0 \left(\frac{\sin \frac{u}{4}}{\frac{u}{4}} \right)^2. \quad (1.10)$$

For this expression the first minimum lies at $u = 4\pi$. Converting back to Cartesian coordinates, the axial resolution can be expressed as:

$$\delta_z = \frac{2n\lambda_0}{NA^2}. \quad (1.11)$$

Up till here, we only considered a single, point-like emitter. In a more realistic scenario, however the emitters are neither point-like, nor single. Effectively, however, for every emitter the PSF would be imaged on the sensor, and this creates the final image. In mathematical terms, this can be expressed as a convolution operation between the underlying fluorophore distribution of the object (O) and the PSF (H):

$$I(u, v) = O(u, v) * H(u, v). \quad (1.12)$$

The effective result of this kind of diffraction limited image formation is a blurred image with a finite resolution of δ_{xy} in the lateral direction, and δ_z in the axial direction.

The PSF is further affected by the illumination pattern as well. Since the number of emitted fluorescent photons are roughly proportional to the illumination intensity, if the illumination has any structure at the order of the detection resolution, it will have an effect on the overall PSF of the system, which can be expressed as:

$$H_{sys} = H_{ill} \cdot H_{det}, \quad (1.13)$$

where H_{ill} is the point spread function of the illumination, and H_{det} is the point spread function of the detection.

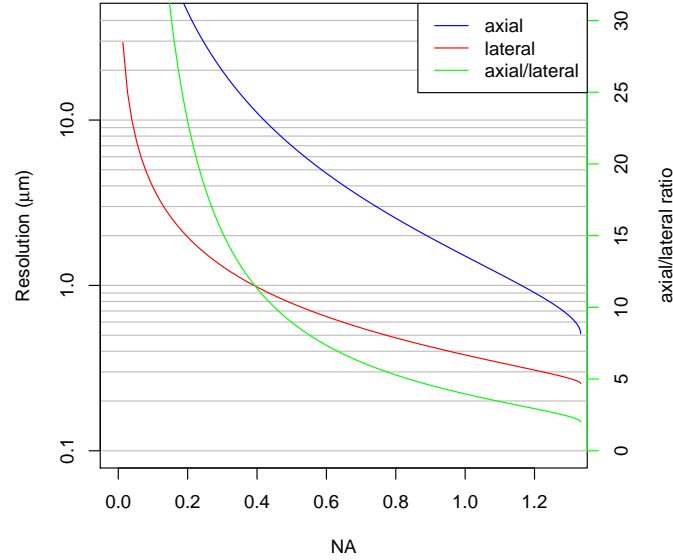


Figure 1.5: Resolution of a wide-field microscope. Axial (blue) and lateral (red) resolutions of a wide-field microscope are shown with respect to the numerical aperture (NA). Resolutions are calculated with $\lambda = 510nm$, the emission maximum of GFP and $n = 1.33$, the refractive index of water, for water dipping objectives.

1.2 Imaging in three dimensions

In most cases, a wide-field microscope is used to image a section of a tissue, thus axial resolution is not a concern. Imaging live specimens, however is not so straightforward, as these samples are usually much thicker than a typical section. For these samples 3-dimensional (3D) imaging is highly beneficial, which necessitates some kind of optical sectioning technique to be able to discriminate the features at different depths.

Due to the design of the wide-field microscope, any photons emitted from outside the focal plane will also be detected by the sensor, however as these are not originating from the focus, only a blur will be visible. This blur potentially degrades image quality and signal to noise ratio to such extent that makes imaging thick sample very difficult if not impossible in a wide-field microscope [!!!].

Evaluating Equations (1.9) and (1.11) for a range of possible numerical apertures reveals the significant differences in lateral and axial resolution for any objective (Fig. 1.5). Especially for low NAs, this can be significant, a factor of ~ 20 difference. For higher (>0.8) NAs the axial resolution increases faster than the lateral, however they will only be equal when $\alpha = 180^\circ$. This means that isotropic resolution with a single lens is only possible, is the lens is collecting all light emitting from the sample, which seems hardly possible, and would be highly impractical. For commonly use high NA objectives the

1. LIGHT-SHEET IMAGING OF MAMMALIAN DEVELOPMENT

lateral to axial ratio will still be around 3–6.

Instead of using a single lens to achieve isotropic resolution, it's more practical to image the sample from multiple directions to complement the missing information from different views. When rotating the sample 90° for example, the lateral direction of the second view will correspond to the axial direction of the first view. If rotation is not possible, using multiple objectives can also achieve similar result, such as in the case of Multi-Imaging Axis Microscopy (MIAM) [44, 45]. This microscope consisted of 4 identical objectives arranged in a tetrahedral fashion to collect as much light as possible from multiple directions, and provide isotropic 3D resolution, albeit at the expense of extremely difficult sample handling, since the sample was completely surrounded by objectives from all directions.

1.2.1 Laser scanning confocal microscopy

Laser scanning confocal microscopy [7, 8] addresses most of the problems of wide-field microscopy we mentioned in the previous section. It is capable of optical sectioning by rejecting out of focus light, which makes it true 3D imaging technique. Furthermore, the light rejection also massively reduces out of focus background, and increases contrast.

This is achieved by two significant modifications compared to the wide-field optical path. To be able to reject the out of focus light, an adjustable pinhole is placed at the focus of the tube lens. Light rays originating from the focal point will meet at this position, and are able to pass through the pinhole, however out of focus light will converge either before or after the aperture, and thus the aperture blocks these rays. To maximize the fluorescence readout efficiency for the single focal point, a photomultiplier tube is used instead of an area sensor (Fig. 1.6a).

To maximize the signal from the focal point, the illumination light is also focused here by coupling an expanded laser beam through the back aperture of the objective. This not only increases illumination efficiency (since other, not detected points are not illuminated), but has the added benefit of increasing the resolution as well. This is due to the combined effect of illumination and detection PSF as described in Eq. (1.13) (Fig. 1.7). For Gaussian-like PSF-s, the final resolution (along a single direction) can be calculated in the following way:

$$\frac{1}{\delta_{sys}^2} = \frac{1}{\delta_{ill}^2} + \frac{1}{\delta_{det}^2}, \quad (1.14)$$

where δ_{ill} and δ_{det} are the resolutions for the illumination and detection respectively. Since the same objective is used for both illumination and detection, and the difference

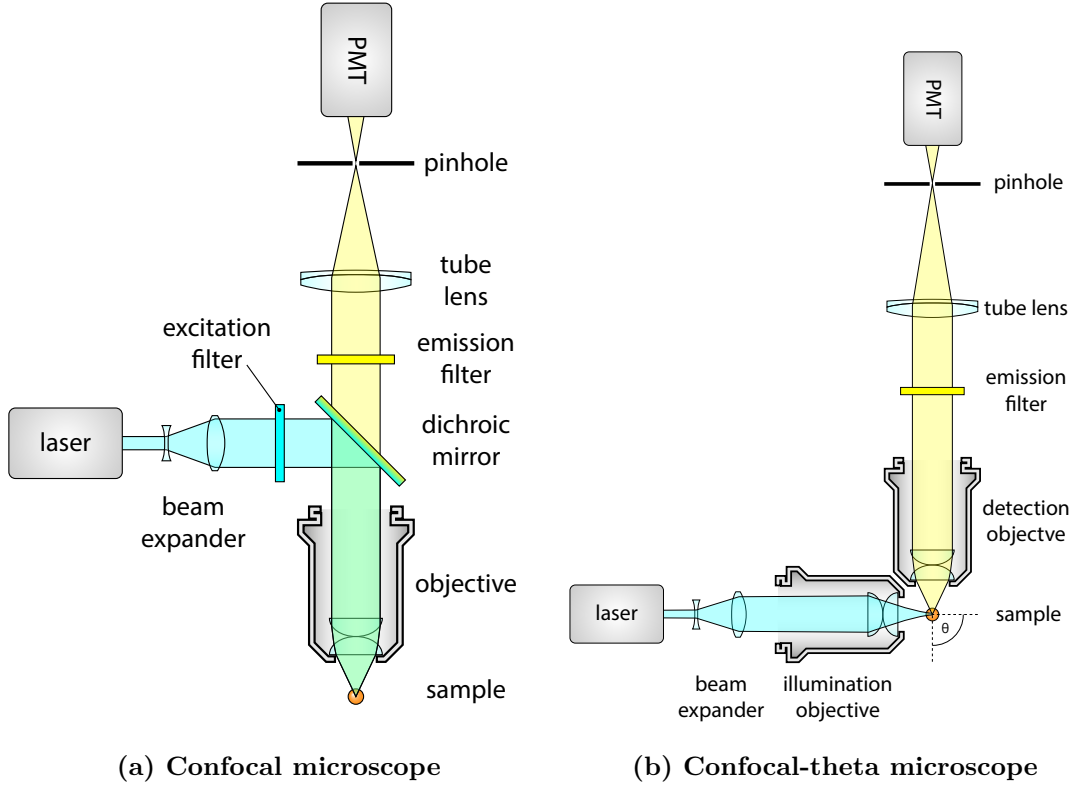


Figure 1.6: Basic optical components of a laser scanning confocal and confocal-theta microscope. Both type of microscopes use confocal images detection, which means that a pinhole is used to exclude light coming from out of focus points. Light intensity is measured by a photomultiplier for every voxel in the region of interest. The final image is generated on a computer using the positions and recorded intensity values. A regular confocal microscope (1.6a) uses the same objective for illumination and detection, while a confocal-theta microscope (1.6b) uses a second objective that is rotated by ϑ around the focus. In this case, $\vartheta = 90^\circ$.

in wavelength is almost negligible, $\delta_{ill} = \delta_{det} = \delta$, the final system resolution will be:

$$\delta_{sys} = \frac{1}{\sqrt{2}}\delta. \quad (1.15)$$

This means that the distinguishable features in a confocal microscope are ~ 0.7 times smaller than in a wide-field microscope using the same objective.

Because of the different detection method in a confocal microscope, direct image formation on an area sensor is not possible, since at any given time, only a single point is interrogated in the sample. Instead, it's necessary to move the illumination and detection point in synchrony (or in a simpler, albeit slower solution, the to move sample) to scan the entire field of view. The image can be later computationally reconstructed by a computer program that records the fluorescence intensity of every point of the field of view, and displays these values as a raster image.

1. LIGHT-SHEET IMAGING OF MAMMALIAN DEVELOPMENT

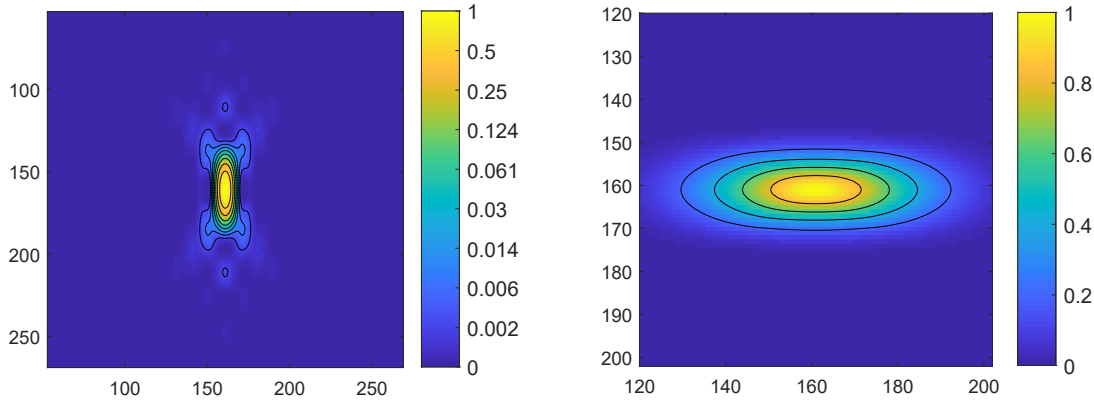


Figure 1.7: Axial cross section of the PSF and OTF of a laser scanning confocal microscope. Simulated PSF and OTF for a laser scanning confocal microscope with a water immersion objective ($n = 1.33$). $NA = 1.1$, $\lambda = 510$ nm

1.2.2 Confocal-theta microscopy

Although confocal microscopy already has 3D capabilities, its axial resolution is still limited compared to the lateral, since it uses only one objective. An alternative realization of the confocal microscope, the confocal theta microscope [46] introduces a second objective to the system, that is used to illuminate the sample (Figure 1.6b). Since this decouples the illumination and detection, using a filter cube is no longer necessary. The second objective is rotated by ϑ around the focus, this is where the name of this setup originates from.

As in the case of standard confocal microscopy, the system PSF is improved by the illumination pattern. Here, however, the axial direction of the detection coincides with the lateral direction of the illumination, which results in a dramatic improvement of axial resolution compared to standard confocal microscopy. Lateral resolution will also be increased, but by a smaller extent, resulting in an almost isotropic PSF, and equal axial and lateral resolution (Fig. ??).

Although this is a big improvement to confocal microscopy in terms of resolution, this technique did not reach a widespread adoption as it complicates sample handling, while still suffering from two big drawbacks of confocal microscopy techniques that limit its live imaging capabilities.

Imaging live specimens for an extended period of time with confocal microscopy although possible [22, 47], is not ideal. For each voxel imaged, a large portion of the specimen has to be illuminated, which results in a very high dose of radiation on the samples. This can be as much as 30–100 times larger, than the dose used for the actual imaging [48]. Illumination with high power of laser for an extended time frame can result in bleaching the fluorophores, which in turn will lower the signal at later times.

Furthermore, any absorbed photon has the possibility to disrupt the chemical bonds inside the specimen, which can lead to phototoxic effects. Furthermore, the usage of the pinhole although increases resolution, also decreases the detectable signal intensity, thus has a negative impact on image contrast [49].

1.3 Light-sheet microscopy

A selective-plane illumination microscope (SPIM) uses a light-sheet to illuminate only a thin section of the sample (Figure 1.8). This illumination plane is perpendicular to the imaging axis of the detection objective and coincides with the focal plane. This way, only the section in focus will be illuminated, thus providing much better signal to noise ratio. In case of conventional wide-field fluorescent microscopy, where the whole specimen is illuminated, light scattering from different regions contribute to a significant background noise. With selective-plane illumination, this problem is intrinsically solved, and it also provides a true sectioning capability. This makes SPIM especially suitable for 3D imaging.

The main principle behind single plane illumination microscopy, that is illuminating the sample from the side by a very thin light-sheet, dates back to the early 20th century, when Siedentopf and Zsigmondy first described the ultramicroscope [50]. This microscope used sunlight as an illumination source, that was guided through a precision slit to generate a thin light-sheet. This allowed Zsigmondy to visualize gold nanoparticles floating in and out of the light-sheet. Since these particles are much smaller than the wavelength of the light, the device was called an ultramicroscope. His studies with

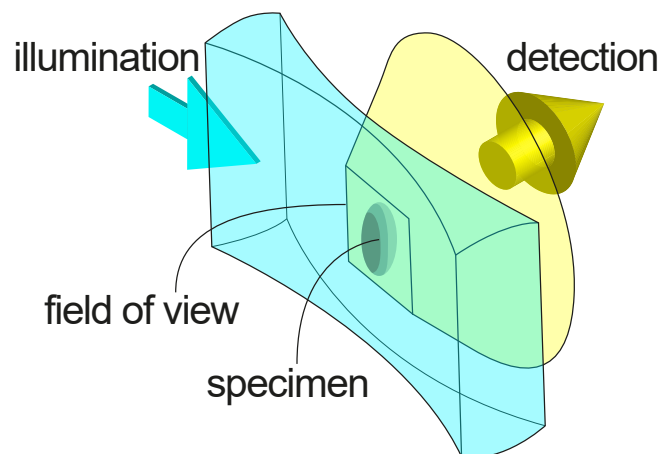


Figure 1.8: Basic concept of single-plane illumination microscopy. The sample is illuminated from the side by laser light shaped to a light-sheet (blue). This illuminates the focal plane of the detection lens, that collects light in a wide-field mode (yellow). The image is recorded, and the sample is translated through the light-sheet to acquire an entire 3D stack.

1. LIGHT-SHEET IMAGING OF MAMMALIAN DEVELOPMENT

colloids together with the development of the ultramicroscope led Zsigmondy to win the Nobel Prize in 1925.

previous to SPIM: Voie et al. fixed guinea pig cochlea, rotating and reconstruction in 3D [51], called Orthogonal-plane Fluorescent Optical Sectioning. Lateral resolution around $10\text{ }\mu\text{m}$ and axial resolution of $26\text{ }\mu\text{m}$, with very large, 1.5 mm field of view. Since the specimens they imaged contained calcium rich bone tissue, optical imaging was only possible by using an optical clearing method. In this work, they used EDTA (ethylenediaminetetraacetic acid) dehydrated in ethyl alcohol, then it was cleared, finally immersed in a fluorescent dye bath. TO acquire 3D images, the specimen was rotated, and translated to compensate for the off-axis rotation.

follow-up to Voie and Spelman: [52] 3D reconstruction of the cochlea for the images

Similar to SPIM but not fluorescent: light scanning photomicrography [53]

Then, in 2002, Fuchs et al. introduces Thin Light-Sheet Microscopy [54] who use this technique to investigate the microbial life in seawater samples without disturbing their natural environment (by e.g. placing them on a coverslip). Using TSLM allowed the to image the bacteria directly in the staining solution containing SYBR Green I without having to deal with background illumination from the dye, which would have been an issue with confocal microscopy for example. Their light-sheet was similar to the one utilized in OPFOS, being $23\text{ }\mu\text{m}$ thin, and providing a $1\text{ mm} \times 1\text{ mm}$ field of view.

The real breakthrough happened when light-sheet microscopy was combined with endogenous fluorescent labels: fluorescent proteins live imaging for long time and light-sheet these techniques were all combined in the 2004 Science paper from Huisken et al. that marks a landmark in light-sheet microscopy, and since then a widespread adoption started in biological research, with multiple groups implementing their own setups.

Since then however, light-sheet microscopy was seldom used, but in the last decade it was reinvented and combined with fluorescent microscopy. The first notable light-sheet fluorescent microscope (LSFM) was developed at EMBL in 2004 [55], that demonstrated the benefits of using a light-sheet in imaging developmental processes in three dimension.

Since then, light-sheet based imaging has gained more and more popularity, as it can be adapted and applied to a wide variety of problems. It was numerously proven to be a better choice than confocal microscopy [48, 56] especially in developmental biological applications [57]. It can also be used with a wide variety of specimens of different sizes, such as zebrafish embryo [58–60], mouse brain [61] or drosophila embryo [26]. It is also possible to use light-sheet microscopy in super-resolution, allowing for individual molecule localization [62].

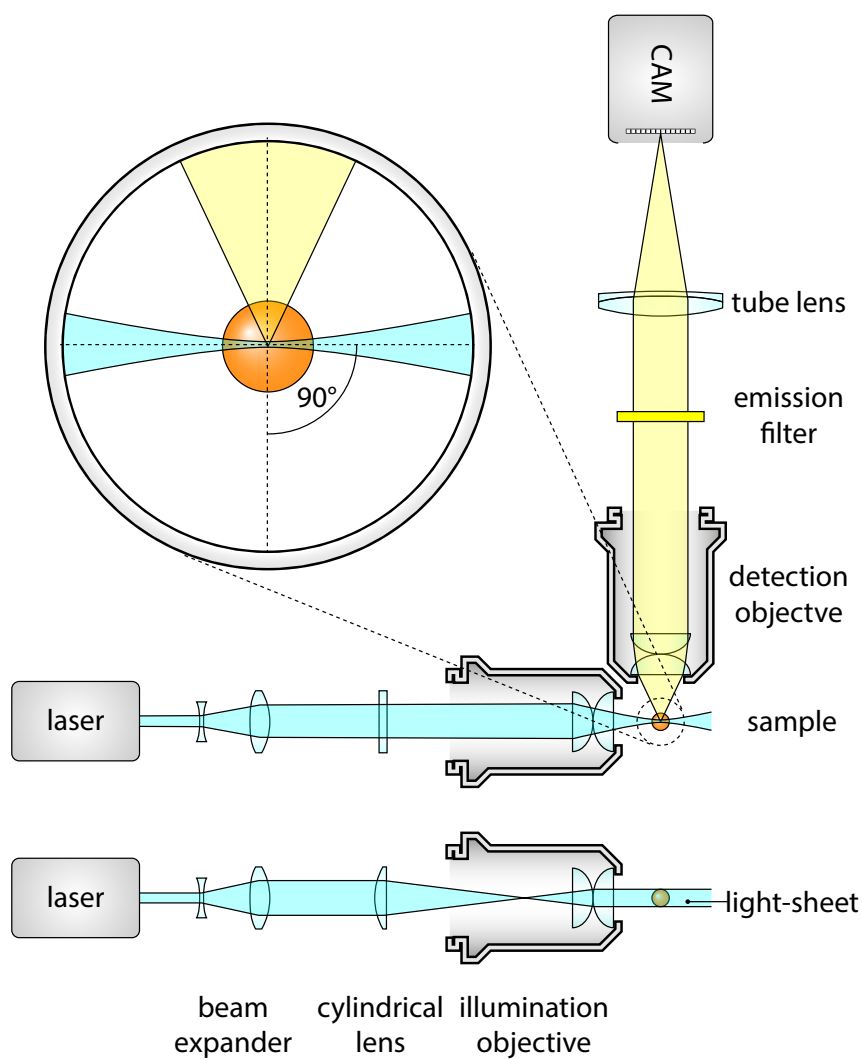


Figure 1.9: Basic optical components of a SPIM. A selective plane illumination microscope uses two objectives orthogonally aligned. One objective is used to generate a thin light-sheet that illuminates the sample from the side, while the other is used for detection. To generate an image of the specimen, a suitable tube lens is used to focus the light on the sensor of a detection unit (e.g. sCMOS camera). The light-sheet is generated by the illumination objective, using a beam that is previously shaped by a cylindrical lens.

1. LIGHT-SHEET IMAGING OF MAMMALIAN DEVELOPMENT

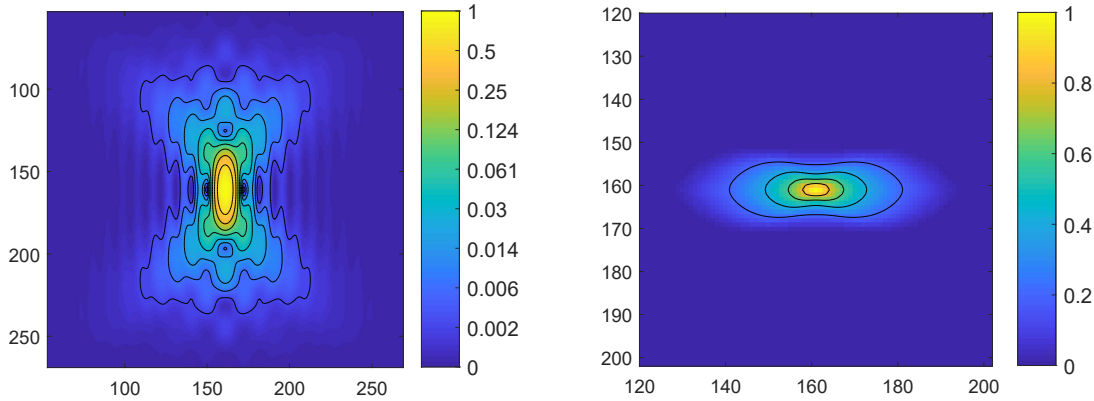


Figure 1.10: Axial cross section of the PSF and OTF of a single plane illumination microscope. Simulated PSF and OTF for a single plane illumination microscope with a water immersion objectives ($n = 1.33$). Detection: $NA = 1.1$, $\lambda = 510$ nm, Illumination: $NA = 0.1$, $\lambda = 488$ nm

1.3.1 Optics of light-sheet microscopy

Since illumination and detection for light-sheet microscopy are decoupled, two independent optical paths are implemented.

The detection unit of a SPIM is basically equivalent to a detection unit of a wide-field microscope, without a dichroic mirror (Figure 1.9). Most important components are the objective together with the tube lens, filter wheel, and a sensor, typically a CCD or sCMOS camera.

One of the most important aspects that determine the resolution of the microscope is the detection objective. Since in developmental biology specimens require a water-based solution, these objectives are usually water dipping objectives directly submerged in the medium. Since the refraction index of water ($n = 1.33$) is greater than the refraction index of air, these objectives tend to have a higher NA , which results in higher resolution. This, however, also depends on the sensor used, mainly on the pixel size (d_{sensor}).

The magnification is typically $10\times$, $20\times$, $40\times$ or $100\times$ but these values are sound only when the objective is used together with the prescribed tube lens. These lenses are specially made to be used with the specific objectives, and are corrected for any aberrations. They typically have a focal length of 160–200mm.

1.3.2 Static light-sheet illumination

The light-sheet can be generated using a cylindrical lens, which focuses the laser beam in only one direction, and creating a thin sheet in the proximity of the focal point. However, to achieve light-sheets that are thin enough, one would need to use cylindrical lens with low focal lengths, but these are hardly accessible in well corrected formats. For this

reason, its more common to use a longer focal length cylindrical lens in conjunction with a microscope objective, which is well corrected for chromatic and spherical aberrations [63]. This way, the light-sheet length, thickness and width can be adjusted for the specific imaging tasks.

For paraxial waves, i.e. waves with nearly parallel wave front normals, a general wave equation can be approximated with the paraxial Helmholtz equation [64, 65]

$$\nabla_T^2 + i2k \frac{\partial U}{\partial z} = 0 \quad (1.16)$$

where $\nabla_T^2 = \frac{\partial^2}{\partial x^2} + \frac{\partial^2}{\partial y^2}$, $U(\vec{r})$ is the wave-function, $k = \frac{2\pi}{\lambda}$ is the wavenumber and we assume, that the light spreads in z direction.

A simple solution to this differential equation is the Gaussian beam:

$$U(r, z) = A_0 \cdot \frac{W_0}{W(z)} \cdot e^{-\frac{r^2}{W^2(z)}} \cdot e^{-i\phi(r, z)} \quad (1.17)$$

where A_0 is the amplitude of the wave, W_0 is the radius of the beam waist (the thinnest location on the beam), $r = \sqrt{x^2 + y^2}$ is the distance from the center of the beam, $W(z)$ is the radius of the beam z distance from the waist, and $\phi(r, z)$ is the combined phase part of the wave-function. Furthermore:

$$W(z) = W_0 \sqrt{1 + \left(\frac{z}{z_0}\right)^2} \quad (1.18)$$

where the parameter z_0 is called the Rayleigh-range. This has the following connection with the beam waist:

$$z_0 = \frac{\pi W_0^2}{\lambda} \quad (1.19)$$

Which means, the thinner the beam waist, the shorter the Rayleigh-range, that is the beam divergence is faster for more focused beams.

Intensity of the emitted fluorescence is based on the intensity of the excitation light. In case of a Gaussian beam:

$$I(r, z) = U(r, z) \cdot U^*(r, z) = |A_0|^2 \cdot \left(\frac{W_0}{W(z)}\right)^2 \cdot e^{-\frac{2r^2}{W^2(z)}} \quad (1.20)$$

Apart from the circular Gaussian beam, the elliptical Gaussian beam is also an eigenfunction of Helmholtz equation (1.16):

$$U(x, y, z) = A_0 \cdot \sqrt{\frac{W_{x,0}}{W_x(z)}} \sqrt{\frac{W_{y,0}}{W_y(z)}} \cdot e^{-\frac{x^2}{W_x^2(z)}} \cdot e^{-\frac{y^2}{W_y^2(z)}} \cdot e^{-i\phi(x, y, z)} \quad (1.21)$$

1. LIGHT-SHEET IMAGING OF MAMMALIAN DEVELOPMENT

This beam still has a Gaussian profile along the x and y axes, but the radii are uncoupled, which results in an elliptical beam. Since the beam waist is different along the two axes, the Rayleigh range is also different:

$$z_{x,0} = \frac{\pi W_{x,0}^2}{\lambda} \quad (1.22)$$

$$z_{y,0} = \frac{\pi W_{y,0}^2}{\lambda} \quad (1.23)$$

Intensity of the beam is the following:

$$I(x, y, z) = U(x, y, z) \cdot U^*(x, y, z) = |A_0|^2 \cdot \frac{W_{x,0}}{W_x(z)} \cdot \frac{W_{y,0}}{W_y(z)} \cdot e^{-\frac{2x^2}{W_x^2(z)}} \cdot e^{-\frac{2y^2}{W_y^2(z)}} \quad (1.24)$$

where

$$W_x(z) = W_{x,0} \sqrt{1 + \left(\frac{z}{z_{x,0}}\right)^2} \quad \text{and} \quad W_y(z) = W_{y,0} \sqrt{1 + \left(\frac{z}{z_{y,0}}\right)^2} \quad (1.25)$$

Since the illumination is uneven, the usable field of view is smaller than the actual illuminated region (Figure 1.11a). The width of the field of view w_{fov} is determined by the Rayleigh length, since this is in a direct relation with the beam divergence. To stay in the optimal region, the light-sheet should only be used in the range of 1 Rayleigh length on both sides of the beam waist (Figure 1.11b). In this range, the ratio between the thickest (at $z = z_0$) and the thinnest (at $z = 0$) part of the beam $W(z)$ will be $\sqrt{2} \approx 1.4142$ which is still acceptable.

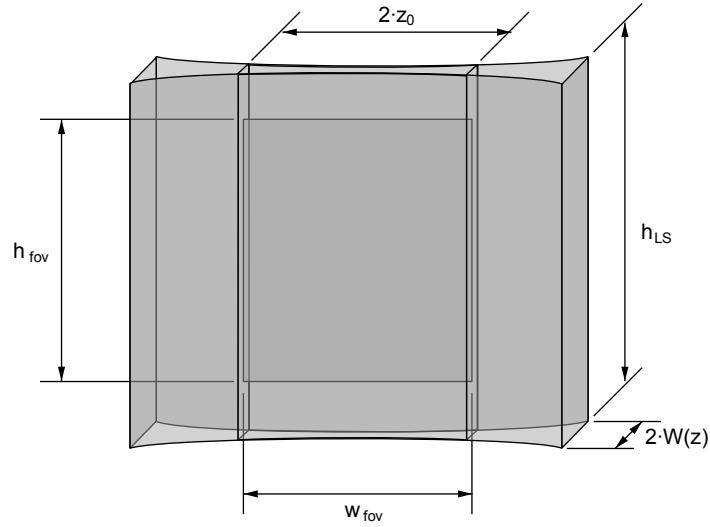
Light-sheet height is determined by the profile of the beam along the vertical axis (Figure 1.11c). Since this is a Gaussian function (see Equation 1.17), only a small part in the middle can be used for imaging, because towards the sides the intensity dramatically drops. To allow a maximum 80% drop of intensity at the edges, the light-sheet height is $h_{fov} = 2 \cdot 0.472 \cdot W_{x,0}$

1.3.3 Digitally scanned light-sheet illumination

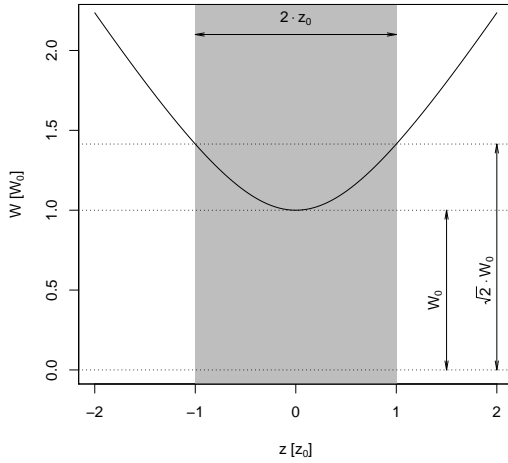
Since using cylindrical lenses it's not possible to generate a homogeneous light-sheet, moreover at higher magnification the Rayleigh range would be too small, we also consider using focused beam scanning to generate the light-sheet (digital scanned light-sheet microscopy, DSLM [58]). To generate a scanning beam, a galvanometer controlled mirror is used to alter the beam path. This can quickly turn around its axis which will result in an angular sweep with the laser beam. To change the angular movement to translation, a scan lens is used to generate an intermediate scanning plane. This plane is then imaged to the specimen by the tube lens and the illumination objective, resulting in a scanned

focused beam.

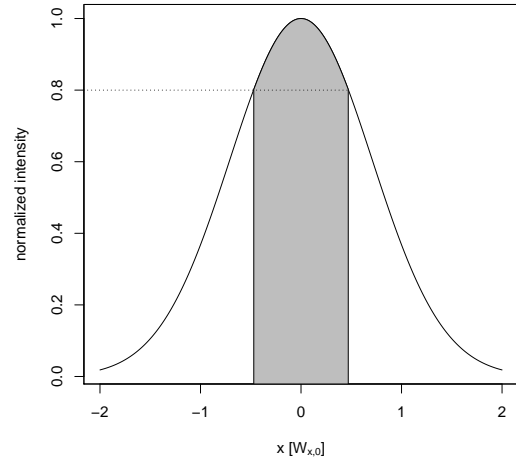
This method to generate the light-sheet has several advantages compared to a static light-sheet. The height of this sheet is not determined by the cylindrical lens, but it can be dynamically modified. Also, the intensity is uniform through the whole height of the light-sheet.



(a)



(b)



(c)

Figure 1.11: Light-sheet dimensions. 1.11a shows a light sheet, with the field of view indicated. Since the light-sheet intensity is uneven, the field of view has to be confined to a smaller region. 1.11b The width and thickness of the field of view depends on the Rayleigh length of the beam ($z_{y,0}$). 1.11c Height of the field of view is determined by the Gaussian profile of the elliptical beam.

1. LIGHT-SHEET IMAGING OF MAMMALIAN DEVELOPMENT

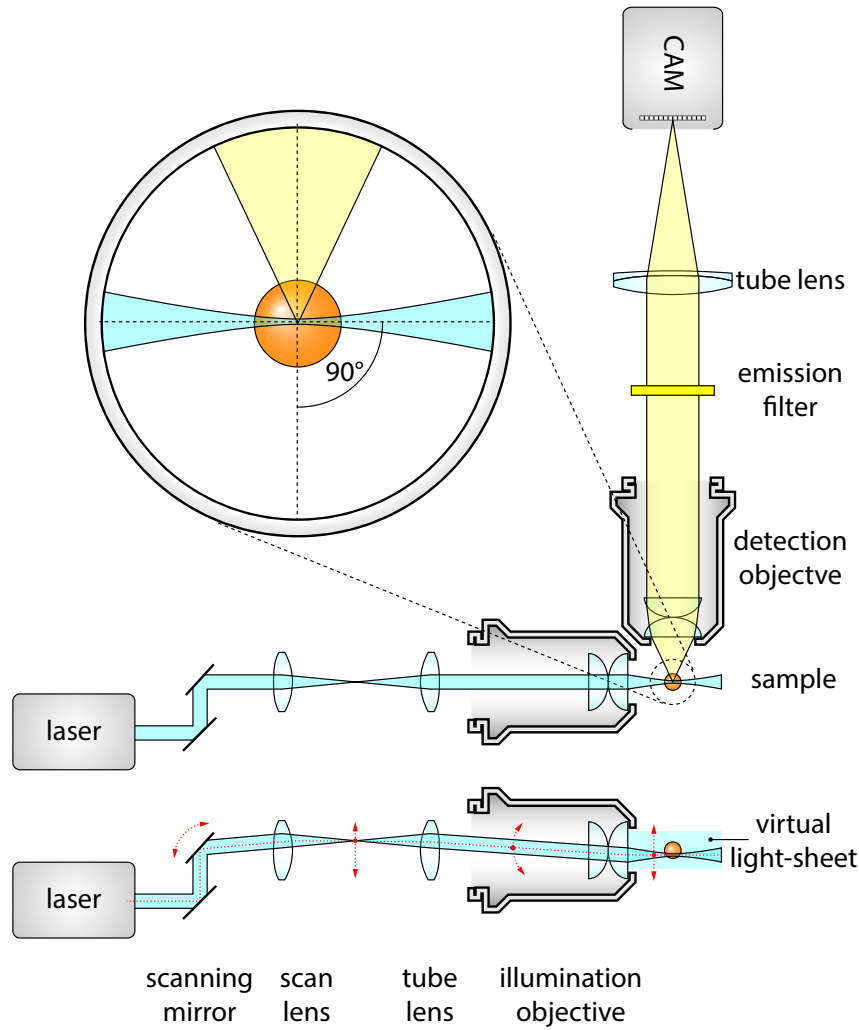


Figure 1.12: DSLM illumination. DSLM illuminates a specimen by a circularly-symmetric beam that is scanned over the field of view. This creates a virtual light-sheet, which illuminates a section of a specimen just like the SPIM. Light-sheet in DSLM is uniform over the whole field of view and its height can be dynamically altered by changing the beam scan range.

1.4 Multi-view light-sheet microscopy

already in 1989 multi-view to increase axial resolution in conventional optical microscope. They imaged *Drosophila* metaphase plate in Zeiss Axiomat microscope using a 63x 1.2 NA water immersion objective lens. To increase the axial resolution, a special rotation stage was constructed, that allowed rotation around the object of interest to image it from a 90° tilted view. Using a fusion method in the Fourier space, the resolution increased to 0.25 μm in lateral and 0.4 μm in the axial direction for real samples.

Multiple imaging axis microscopy (MIAM) [44] to image specimens from 4 directions in a tetrahedral objective configuration, could reach a 5.8 fold increase in axial resolution

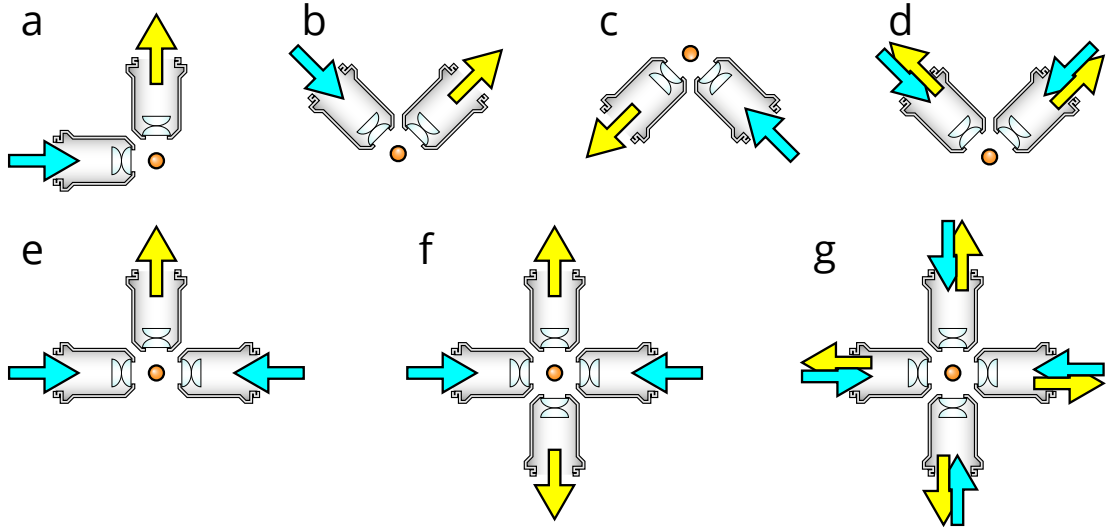


Figure 1.13: Different optical arrangements for light-sheet microscopy. (a) Original SPIM design with a single lens for detection and illumination. [55] (b) Upright SPIM to allow for easier sample mounting such as using a petri dish (iSPIM, [67, J2]). (c) Inverted SPIM, where the objectives are below the sample, which is held by a thin foil [J1]. (d) Dual-view version of the upright configuration, where both objective can be used for illumination and detection (diSPIM, [68]). (e) Multidirectional-SPIM (mSPIM) for even illumination of the sample with two objectives for illumination [69]. (f) Multi-view SPIM with two illumination and detection objectives for *in toto* imaging of whole embryos (MuVI-SPIM [26], SimView [27], Four-lens SPIM [70]). (g) A combination of (d) and (f), using 4 identical objectives, where both can illuminate and detect in a sequential manner, to achieve isotropic resolution without sample rotation (IsoView [71]).

by combining the four views as a weighted average. Follow up for this: sample manipulation with optical tweezers / optical levitation in 3D [66](because of the lack of space for mechanical translation stage) positioning of a 20 μm latex bead in a 100 μm diameter volume by changing the intensity of 4 laser beams.

things to improve: resolution axial resolution relative to lateral complete view reduce scattering

1.5 Image processing for multi-view microscopy

When using any kind of microscopy in research, image processing is a crucial part of the workflow. This is especially true for light-sheet microscopy, since it's capable imaging the same specimen for multiple days, producing immense amounts of data. A single overnight experiment of *Drosophila* development (which is a very typical use-case for light-sheet) can produce multiple terabytes of data. To see the real scales, let's consider the following imaging conditions:

1. LIGHT-SHEET IMAGING OF MAMMALIAN DEVELOPMENT

camera	Hamamastu Orca Flash 4
image size	8 MB
1 stack = 250 planes	2 GB
2 views	4 GB
Time-lapse: 16 h @ 2/min	7.5 TB
n colors	$n \cdot 7.5$ TB

As it is apparent from this table,

1.5.1 Registration

Image based registration

Bead based registration

1.5.2 Transformation

Rigid

Affine

Elastic

1.5.3 Image fusion

Average

Sigmoidal weighted average

Fourier mixing

Huisken had something like this

Wavelet-based fusion

Multi-view deconvolution

[64] Uros thesis [72], [73] Spatially variant deconvolution

1.6 Image compression

Image compression is an important tool for everyday life, however it's rarely used in the context of scientific imaging because of fear of information loss. This preconception is mainly due to the famous blocking artifacts found in many highly compressed JPEG images, however not all image compression algorithms introduce artifacts, and in fact many lossless algorithms exist that would be suitable for such images. Nowadays, when data production is in an exponential growth compression is again in highlight, without it

it would be extremely difficult to maintain many scientific projects that produce images at a high data rate.

In this paper I will review the basics of image compression based on Sayood's textbook, Introduction to Data Compression [74]. I will introduce some basics of information theory and entropy, followed by discussing two widely used entropy coding algorithms, Huffman coding and arithmetic coding. Section 3 will be about transform coding, specifically Discrete Cosine Transform (DCT) and wavelet transform while also touching upon techniques based on differential pulse code modulation. Finally I will show how some of the most widely used image compression standards use these methods to achieve effective image compression.

1.6.1 Entropy coding

Information and Entropy

For the purpose of data compression it is useful to quantify the amount of *information* contained within a piece of data. The first rigorous definition of information was presented in an extremely influential paper by Shannon, published in two parts in 1948 [75, 76].

First, let's define the amount of self-information contained in the outcome of a random experiment:

$$I(A) = \log_b \frac{1}{P(A)} = -\log_b P(A) \quad (1.26)$$

2 independent events:

$$P(A, B) = P(A) \cdot P(B) \quad (1.27)$$

self-information is additive:

$$I(A, B) = \log_b \frac{1}{P(A, B)} \quad (1.28)$$

$$= \log_b \frac{1}{P(A) \cdot P(B)} \quad (1.29)$$

$$= \log_b \frac{1}{P(A)} + \log_b \frac{1}{P(B)} \quad (1.30)$$

entropy for random variable X average or expected self-information for the random variable

$$H(X) = \sum_i P(A_i) I(A_i) = - \sum_i P(A_i) \log_b P(A_i) \quad (1.31)$$

entropy rate for data source S average information output by the data source

1. LIGHT-SHEET IMAGING OF MAMMALIAN DEVELOPMENT

Table 1.1: Examples of a random binary code (#1) and a prefix-free binary code (#2). Code #2 is uniquely decodable, while for code #1 it's necessary to introduce boundaries between codewords to be able to distinguish them.

Letter	Code #1	Code #2
a_1	0	10
a_2	11	11
a_3	00	00
a_4	10	010
a_5	111	011

Huffman coding

Huffman coding is a prefix-free, optimal code that is widely used in data compression. It was developed by David A. Huffman as a course assignment on the first ever course on information theory at MIT, and was published shortly afterwards [77]. It is a variable length binary code which assigns different length codewords to letters of different probabilities. It is able to achieve optimal compression, which means the total length of the coded sequence will be minimal.

Although it produces a variable length code which can introduce some issues with decoding, it is still uniquely decodable. It achieves this property by using prefix-free codewords, meaning that none of the codewords are prefixes of any other codewords. This property can be exploited when decoding the codeword, since during this procedure the number of bits for the next codeword can not be determined in advance. However if no codeword is a prefix of another codeword, by simply reading the successive bits one by one until we reach a valid codeword, it's possible to uniquely decode the message.

Let's take the example in Table 1.2. Five letters are coded in binary code by Code #1 and by Code #2. Code 1 is not a prefix code, and because of this when reading the encoded sequence we can not be sure when we reach the end of a codeword. Decoding the sequence 0000 for example could be interpreted as 4 letters of a_1 or 2 letters of a_3 .

The Huffman coding procedure is based on two observations regarding optimal and prefix-free codes:

1. For a letter with higher frequency the code should produce shorter codewords, and for letters with lower frequency it should produce longer codewords.
2. In an optimum code, the two least frequent codewords should have the same lengths.

From these statements the first is trivial to see that is correct. If the more frequent letters would have longer codewords then the less frequent letters, the average codeword length (weighted by the probabilities) would be larger than in the opposite case. Thus, more frequent letters must not have longer codewords than less frequent letter.

Table 1.2: Huffman code table.

Letter	Probability	Codeword
a_2	0.4	$c(a_2)$
a_1	0.2	$c(a_2)$
a_3	0.2	$c(a_2)$
a_4	0.1	$c(a_2)$
a_5	0.1	$c(a_2)$

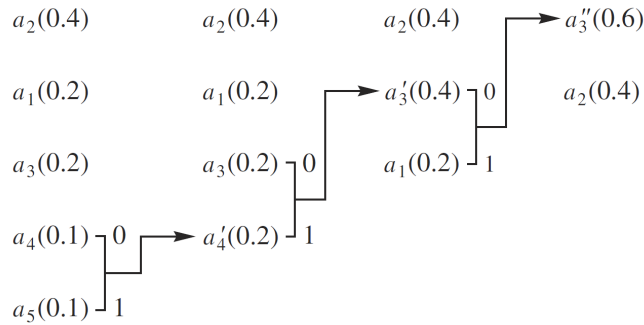


Figure 1.14: Building the binary Huffman tree. The letters are ordered by probability, these will be the final leaf of the tree. To join the to branches at every iteration we join the to nodes with the smallest probability, and create a new common node with the sum of the probabilities. This process is continued until all nodes are joined in a root node with probability of 1. Now, if we traverse down the tree to each leaf, the codeword will be defined by their position.

The second statement at first glance might be so intuitive, so let's consider the following situation. The two least frequent codewords do not have the same lengths, that is the least frequent is longer. However, because this is a prefix code, the second longest codeword is not a prefix of the longest codeword. This means, if we truncate the longest codeword to the same length as the second longest, they will still be distinct codes and uniquely decodable. This way we have a new coding scheme which requires less space on average to code the same sequence as the original code, from which we can conclude the original code was not optimal. Therefore, for an optimal code, statement 2 must be true.

To construct such a code, the following iterative procedure can be used. Let's consider an alphabet with five letters $A = [a_1, a_2, a_3, a_4, a_5]$ with $P(a_1) = P(a_3) = 0.2$, $P(a_2) = 0.4$ and $P(a_4) = P(a_5) = 0.1$ (Table 1.2). The entropy for this source is 2.122 bits/symbol. Let's order the letters by probability, and consider the two least frequent. Since the codewords assigned to these should have the same lengths, we can assign their codewords as

$$c(a_4) = \alpha_1 * 0$$

$$c(a_5) = \alpha_1 * 1$$

1. LIGHT-SHEET IMAGING OF MAMMALIAN DEVELOPMENT

Table 1.3: Huffman code table.

Letter	Probability	Codeword
a_2	0.4	1
a_1	0.2	01
a_3	0.2	000
a_4	0.1	0010
a_5	0.1	0011

where $c(a_i)$ is the assigned codeword for letter a_i and $*$ denotes concatenation. Now we define a new alphabet A' with only four letters a_1, a_2, a_3, a'_4 , where a'_4 is a merged letter for a_4 and a_5 with the probability $P(a'_4) = P(a_4) + P(a_5) = 0.2$. We can continue this process of merging the letters until all of them are merged and we have only one letter left. Since this contains all of the original letter, its probability is 1. We can represent the end result in a binary tree (see Figure 1.14), where the leaves are the letter of the alphabet, nodes are the merged letters, and the codewords are represented by the path from the root node to each leaf (compare with Table 1.3). The average length of this code is

$$l = 0.4 \times 1 + 0.2 \times 2 + 0.2 \times 3 + 0.1 \times 4 + 0.1 \times 4 = 2.2 \text{ bits/symbol} \quad (1.32)$$

A measure of the efficiency of this code is its redundancy—the difference between the entropy and the average length. In this case, the redundancy is 0.078 bits/symbol. The redundancy is zero when the probabilities are negative powers of two.

Arithmetic coding

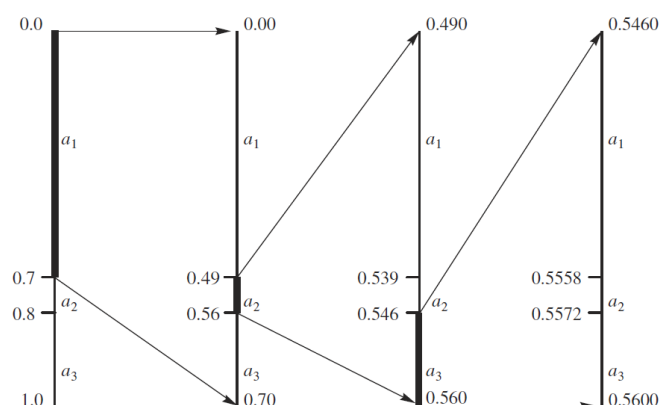
Although in this case the redundancy of the Huffman code is minimal, however in cases where a few symbols have vary high probability compared to the rest, the redundancy increases. This is simply because even for the most frequent letter the shortest codeword the Huffman code can produce is of length 1.

Let's consider the following example: take alphabet $A = [a_1, a_2]$ with $P(a_1) = 0.95$ and $P(a_2) = 0.05$. The first order entropy for this source is $-0.95 \log 0.95 - 0.05 \log 0.05 = 0.2864$ bits/symbol, however if we assign the Huffman code we will have to use $c(a_1) = 0$ and $c(a_2) = 1$, which means the average length will be 1 bit/symbol. This means in order to code this sequence using a Huffman code, we will need more than 3 times the number of bits promised by the entropy.

To get around this fundamental limitation, a coding scheme must be used which does not use discrete codewords at all. Arithmetic coding is the most well-known example of such a scheme. The idea is due to Peter Elias. He developed it during the same course

Table 1.4: Example alphabet for arithmetic coding.

Letter	Probability
a_1	0.7
a_2	0.1
a_3	0.2

Figure 1.15: Arithmetic coding scheme in practice with the alphabet from Table 1.4 on the sequence a_1, a_2, a_3 .

on information theory in which Huffman developed his coding method, but he never published it.

In order to distinguish a sequence of symbols from another sequence of symbols we need to tag it with a unique identifier. One possible set of tags for representing sequences of symbols are the numbers in the unit interval $[0, 1]$. Because the number of numbers in the unit interval is infinite, it should be possible to assign a unique tag to each distinct sequence of symbols. In order to do this, we need a function that will map sequences of symbols into the unit interval.

A straightforward algorithm to arithmetically encode a given input string is the following: Partition the unit interval $[0, 1]$ into sub-intervals and assign one subinterval to each symbol in the input alphabet. The sizes of the sub-intervals are chosen to be proportional to the symbol frequencies. A string of symbols can be encoded by applying this process recursively: The sub-interval from the previous step is subdivided again using the same proportions. Figure 1.15. shows an example of arithmetic coding using the symbol frequencies given in Table 1.4.

This kind of coding although easy to understand, it's actually quite cumbersome to directly implement on a computer, where only a certain floating point precision can be achieved. For real life use this precision is often unsatisfactory, so some extra steps are involved in the coding.

Since after each step the next subinterval is a subset of the previous interval, if the

1. LIGHT-SHEET IMAGING OF MAMMALIAN DEVELOPMENT

coding interval after a certain number of steps is contained in either the upper or lower half of the unit interval it will remain there for the rest of the coding. We can exploit this fact by rescaling that interval to the unit interval and writing either a 0 or 1 bit to the output depending on the position of the subinterval. By continuing this scheme it's possible to reach arbitrary precision even using a computer.

The decoding process is analogous to encoding. The decoder keeps track of the current lower and upper bounds. It mimics the rescaling operations of the encoder based on the bits of the encoded binary number.

1.6.2 Transform coding

The methods outlined in the previous section are effective at compressing the data in an optimal way and reaching the first order entropy, however they assume nothing about the structure of the data. For image compression it's important to also consider this, since most images have a relatively high level of autocorrelation, meaning that neighboring values have a high chance of being similar, although not necessarily equal. Transform coding is a technique that by itself does not compress the data, however by exploiting some knowledge of the structure it transforms the data effectively reducing its first order entropy. When regular entropy coding is then performed on the transformed data, because of the reduced first-order entropy, these techniques can achieve a higher rate of compression. At decompression, after decoding the entropy coder, the reverse transformation is applied to reveal the original data. In this section I will introduce two of the most important algorithms for transform coding, Discrete Cosine Transform and Wavelet Transform.

Discrete Cosine Transform

Discrete Cosine Transform [78] is closely related to the well known Fourier transform. The main idea behind this is to represent a function by a weighted sum of different sine and cosine functions. This provides a different view, instead of looking at the data in the time domain, we gain information about the frequencies that compose the signal.

Discrete Cosine Transform is a variant of the discrete Fourier transformation, however instead of making the signal periodic which can introduce large jumps at the edges, the signal is extended in a symmetric way. Since this will give a smooth transition even at the boundaries, the transform does not have to include so many high frequency components. Also, because of the symmetric extension, it's possible to represent the functions only by using the cosine bases, resulting in fewer coefficients. Overall, the DCT is much better suited for compression, than DFT.

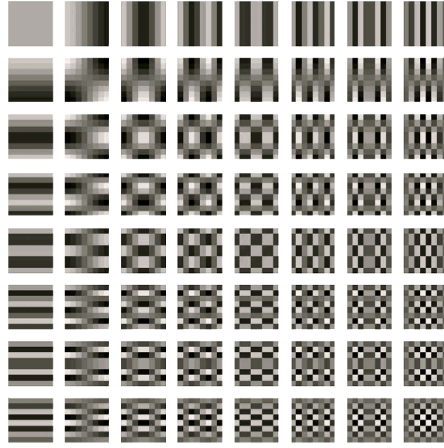


Figure 1.16: Basis functions of the 8×8 2D DCT, computed as the outer product of the 1D basis vectors..

The DCT base functions are defined in the following way:

$$c_{i,j} = s_i \cdot \cos \frac{(2j+1)i\pi}{2n} \quad \text{with } s_i = \begin{cases} \sqrt{\frac{1}{n}} & \text{if } i = 0 \\ \sqrt{\frac{2}{n}} & \text{otherwise} \end{cases} \quad (1.33)$$

The scaling factors are chosen so that the L_2 norm of each basis vector is 1 and so the transform is orthonormal. The inverse transform can therefore be found by simply transposing the transform matrix.

Applying the DCT to two dimensional functions, i.e. images is very similar to the two dimensional Fourier transform. The base functions are the outer products of the 1D base functions (Figure 1.16.), and the transform can actually be performed separately for each dimension.

Computation effort in a naive implementation is $O(n^2)$ but since DCT is based on the Fourier transform, an $O(n \log n)$ algorithm is also possible, analogous to the fast Fourier transform. This is still larger than a linear scaling with the data size, which can be very inconvenient. Therefore, in practice the DCT is usually applied to smaller blocks of the image, such as 4×4 , 8 or 16×16 .

Although DCT is an effective way of reducing the first-order entropy, it has a potential shortcoming by its use of floating point arithmetic. Because of the finite machine precision inherent rounding errors will occur, which means the reverse transformation can not generate the exact original data. For many applications, such as photography, this still can be acceptable, but for scientific image data lossy compression is generally not accepted.

1. LIGHT-SHEET IMAGING OF MAMMALIAN DEVELOPMENT

Discrete Wavelet Transform

Methods based on Fourier analysis, such as the DCT introduced in the previous section, give excellent localization in frequency space: They tell us exactly which frequencies occur in the data, which is very useful for data compression. However, they give no spatial localization: They do not tell us where in the signal these frequencies occur. Every DCT base function affect the whole image domain, which means distinct local structures can have a global effect on the final outcome. In case of an edge for example, it's necessary to include a high frequency component with a large coefficient, but since every DCT base function has an impact on the whole domain, this will have to be compensated on smoother regions by also increasing the coefficients of other factors. This can negatively impact compression performance.

A solution for this is to use different base functions, namely ones with finite support. This way we will not only be able to get information about the frequency, but also about the localization of that frequency in some extent.

One option for such a set of local basis functions, and certainly the most popular one, is the multi-resolution analysis based on wavelets. The term “multi-resolution analysis” in the context of wavelets was introduced in the late 1980s by Stéphane Mallat [79], though research on wavelets had been ongoing for several years before that.

The idea behind the wavelet multi-resolution analysis is to build a basis out of translated and scaled versions of one underlying function called the *mother wavelet* ψ . The mother wavelet is non-zero only in a small region, leading to the locality properties. It is translated to cover the whole domain. It also covers only a small frequency band, and is scaled to cover higher or lower frequencies. The family of translated and scaled functions $\psi_{l,i}$ is generated from according to

$$\psi_{l,i}(t) = \sqrt{2^l} \psi(2^l t - i), \quad l, i \in \mathbb{Z} \quad (1.34)$$

Incrementing l halves the width of the resulting function, which thus corresponds to a higher frequency band. Changing i moves the function along the x axis. The size of each step scales with the width of the function, defined by l . The normalization factor $\sqrt{2^l}$ is chosen so that the L_2 norm stays constant. The mother wavelet can be chosen so that the $\psi_{l,i}$ are pairwise orthogonal and thus form a basis of some function space. However, representing a function in this basis will generally require an infinite number of basis functions $\psi_{l,i}$: To represent a constant component, i.e. content of frequency zero, the wavelet must be infinitely scaled. To address this, it is necessary to introduce an additional scaling function ϕ which complements the wavelet. It is scaled and translated the same way as the mother wavelet.

The oldest wavelets are the Haar wavelets, and because of their simplicity, they

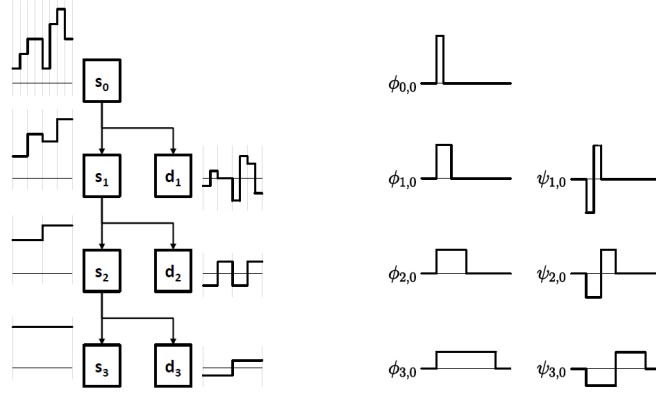


Figure 1.17: Multi-resolution wavelet decomposition, using the Haar wavelets as an example. Left: decomposition to multiple levels of low pass and high pass coefficients corresponding to the scaling and the wavelet functions respectively. Right: some of the base wavelet functions used for the decomposition.

provide a good example on how wavelet transformation works. The Haar wavelet scaling ϕ and wavelet ψ functions are the following:

$$\phi(t) = \begin{cases} 1 & \text{if } 0 \leq t < 1 \\ 0 & \text{otherwise} \end{cases} \quad (1.35)$$

$$\psi(t) = \begin{cases} -1 & \text{if } 0 \leq t < \frac{1}{2} \\ 1 & \text{if } \frac{1}{2} \leq t < 1 \\ 0 & \text{otherwise} \end{cases} \quad (1.36)$$

Clearly, all wavelet functions $\psi_{l,i}$ are orthogonal. Additionally, the scaling functions $\phi_{l,i}$ at a fixed level i are orthogonal. The scaling functions $\phi_{l,i}$ are also orthogonal to the wavelet functions $\psi_{k,i}$, $k \geq l$ at the same and all finer levels.

Figure 1.17. (left) schematically shows the decomposition of a signal into low-pass components corresponding to the scaling function, and high-pass components corresponding to the wavelet. The signal s_0 can be represented by the translated scaling function at a finer scale l_0 , which can be decomposed to the sum of a coarser approximation s_1 corresponding to the scaling function and the detail part d_1 corresponding to the wavelet functions. This decomposition to a sum of coarser approximation and detail can be continued multiple times, thus resulting in the previously mentioned multi-resolution analysis.

Of course, for image compression applications, it is desirable to extend this transformation to a 2D version, that can be applied to the images before performing the arithmetic coding. Similarly to the DCT, the wavelet transform is also separable, and can be performed as a sequence of 1D transforms along different directions. Separable in a sense, that it does not matter in which order the individual 1D DWTs are applied to

1. LIGHT-SHEET IMAGING OF MAMMALIAN DEVELOPMENT

get the same 2D transformation.

JPEG [80], JPEG-LS [81] and JPEG2000

1.6.3 Differential pulse code modulation / LOCO-I?

Chapter 2

Dual Mouse-SPIM

2.1 Previous Mouse-SPIM

mammalian development chromosome segregation cell specification symmetry breaking
signaling pathways human infertility congenital diseases

current mouse-SPIM [J1] already is very good for answering many of these questions

advantages: immersion liquid and culture medium separated open-top sample holder
allow standard microdrop *in vitro* embryo culture row of embryos - high throughput dual
color imaging environmental chamber allows live imaging for 3 days, every

follow chromosomes by tracking kinetochores

from lattice paper: “because photodamage mechanisms that scale supralinearly with
peak intensity have been identified for both visible [82] and two-photon [83] excitation.”

2.2 Light collection efficiency of an objective

Resolution is not the only parameter of concern when designing a new microscope setup.
We also have to consider light collection efficiency, since many application, especially
live imaging applications require a tight photon budget. This means a single fluorophore
can only emit so many times before it undergoes an irreversible chemical reaction, i.e. it
bleaches. The more we can collect of these photons, the more information we gain, and
altogether the efficiency is higher.

Photon collection efficiency also defines single molecule localization accuracy, since
the signal to noise ratio will depend on the square of the number of collected photons.
This is why it’s important to also maximize light collection efficiency.

Let’s define light collection efficiency η as the ratio of collected photons and all
emitted photons:

$$\eta = \frac{N_{collected}}{N_{emitted}}$$

2. DUAL MOUSE-SPIM

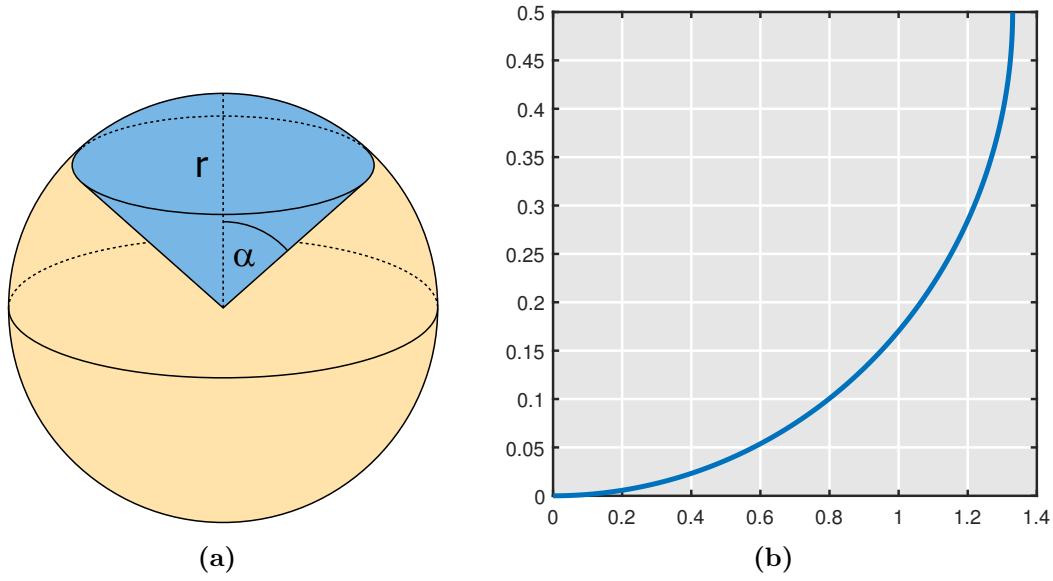


Figure 2.1: Light collection efficiency of an objective. (a) Light collection efficiency is the ratio of photons collected by the objective and all emitted photons. If the fluorophores are emitted randomly in all directions, it will be the surface ratio of the conical section (blue) to the whole sphere. (b) Light collection efficiency (η) as a function of the numerical aperture (NA)

Since we can assume that the direction of photons emitted from a fluorescent molecule are random, the light collection efficiency will correspond to the solid angle subtended by the objective front lens at the focal point. To calculate this, let's consider the unit sphere centered at the focal point, and calculate the surface area of the spherical cap corresponding to the objective acceptance angle α (Fig. 2.1a). The area of the cap can be expressed as a function of the angle:

$$A_{cap} = 2\pi r^2(1 - \cos \alpha)$$

The surface area of the full sphere is calculated as:

$$A_{sph} = 4\pi r^2$$

For both equations r is the radius of the sphere. From here, the light collection efficiency can be calculated as:

$$\eta = \frac{N_{collected}}{N_{emitted}} = \frac{A_{cap}}{A_{sph}} = \frac{1 - \cos \alpha}{2}$$

Some more calculations: (Fig. 2.1b).

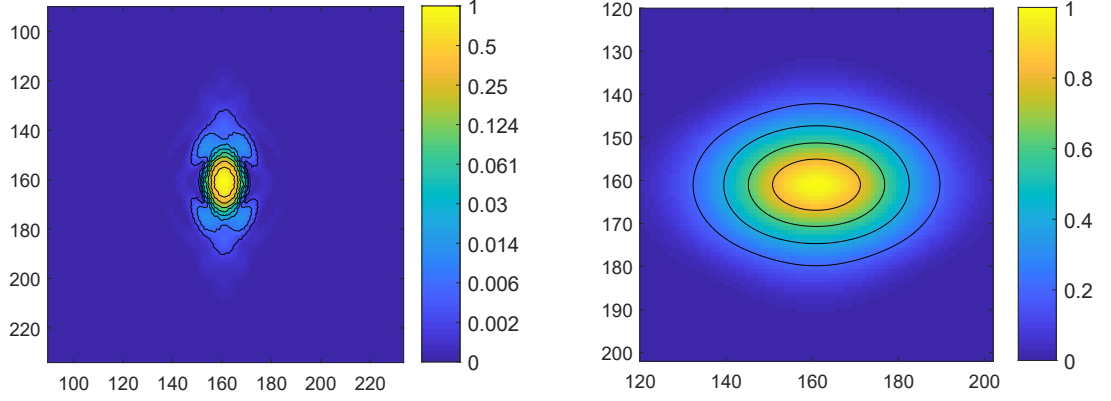


Figure 2.2: Axial cross section of the PSF and OTF of a multi-view single plane illumination microscope. Simulated PSF and OTF for a single plane illumination microscope with a water immersion objectives ($n = 1.33$). Multi-view image acquisition at 120° was simulated. Detection: $NA = 1.1$, $\lambda = 510$ nm, Illumination: $NA = 0.1$, $\lambda = 488$ nm

2.3 Optical layout

design principles: highest isotropic resolution, highest light collection efficiency possible
 2×0.8 NA water dipping in 90° multi-view deconvolve Gaussian fit $\sigma_{xyz} = 135$
 2×1.1 NA water dipping in 120° multi-view deconvolved Gaussian fit $\sigma_z = 135$, and $\sigma_{xy} = 82.2$
simulations from PSF generator! put here

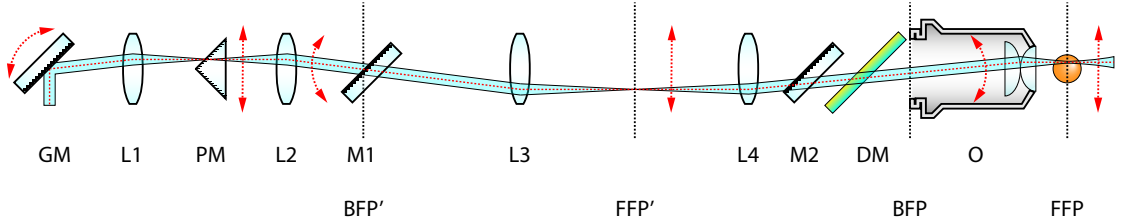


Figure 2.3: Simplified schematics for illumination.

When designing the optical layout of the setup, we had two principles in mind: simplicity and efficiency. Because of the symmetrical design it is possible that

2.4 Optical alignment

Precise alignment of the illumination and detection paths are crucial for high quality imaging, and has a pronounced importance for high magnification and high resolution optical systems. The DualMouse SPIM contains two illumination and detection paths that share many common elements, which makes alignment a *important?* process. The final aim for the alignment is to perfectly overlap the light-sheets with the detection focal

2. DUAL MOUSE-SPIM

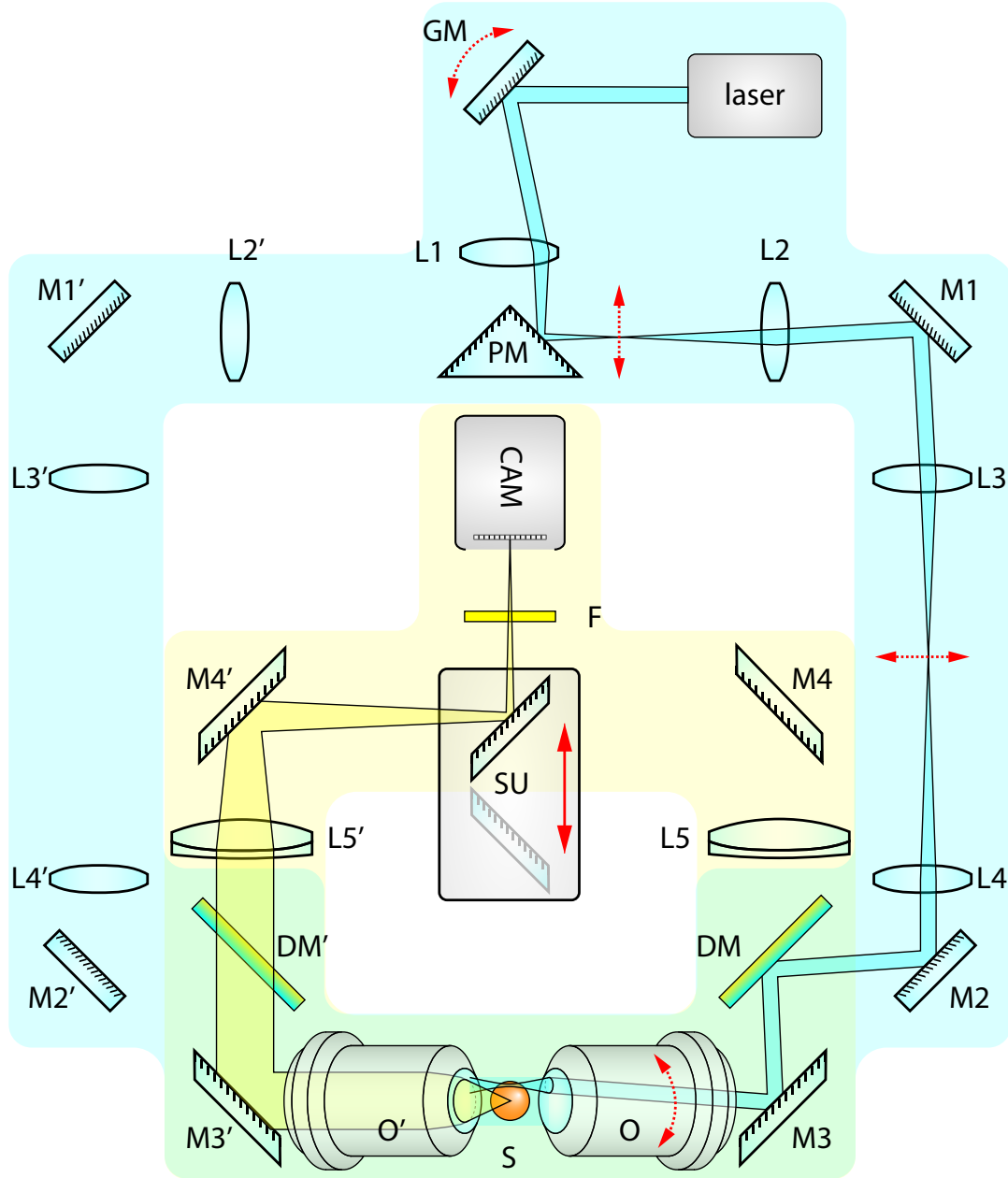


Figure 2.4: Dual Mouse SPIM optical layout. The microscope consists of two main parts, the illumination branches (blue) and detection branches (yellow). For both illumination and detection there are two identical paths implemented. Illumination direction can be changed by applying a different offset to the galvo mirror, which in turn will direct the beam to the opposite face of the prism mirror. L1 and L2 will then image the galvo on M1. Using L3 as a scan lens, and L4 as a tube lens, the scanned beam is coupled to the objective path by quad band dichroic mirror (DM) CAM – camera, DM – dichroic mirror, F – filter wheel, L – lens, M – mirror, O – objective, PM – prism mirror, S – sample, SU – switcher unit

planes, and to optimize ...

2.4.1 Alignment of illumination branches

The two illumination branches start with a common light source, a single mode fiber coupled to laser combiner, and they also share a galvanometric mirror that performs the beam scanning to generate the virtual light-sheet. Likewise shared is a scan lens focusing on the galvo mirror (GM), and the illumination splitter unit (PM, see Section ??).

Alignment for the illumination arms are done in three steps. First the laser beam is aligned on the first rail that holds the galvo, lens L1, and the splitter unit PM. This is performed by two kinematic mirrors placed between the fiber output and the galvo mirror. Using these two mirrors it's possible to freely align the beam along all 4 degrees of freedom: translation in two orthogonal directions, and rotation around two orthogonal axes. Beam alignment on the rail is tested by two irises at the two ends of the rail, if the beam passes through both of them we consider it centered and straight on the optical axis.

After the beam is aligned on the first rail, lens L1 and the splitter unit PM are placed in the measured positions to image the galvo mirror on mirror M1 using lenses L1 and L2. Correct positioning of the splitter unit along the rail is crucial, since this will affect the lateral position and tilt of the beam exiting the unit. To some extent, this can also be compensated by adjusting the two mirrors before the galvo mirror, but is avoided if possible as this will also displace the beam from the center of the galvo mirror.

Adjusting beam position.

Beam position can be adjusted by either translating the beam in a conjugated image plane, or by rotating the beam in a conjugated back focal plane. The setup was designed in a way, that BFP' coincides with mirror M2. This mirror is mounted in a gimbal mirror mount, allowing to rotate the mirror exactly around its center, which avoids unwanted translational movements, and results in pure rotation of the beam. Lens L3 is positioned exactly 1 focal length from the mirror, thus acting as a scan lens, and transforming the rotational movements to translation. This translation is further imaged and demagnified by the tube lens L4 and the objective O.

Adjusting beam tilt Beam tilt can be adjusted by

Adjusting beam axial position.

Adjusting scanning plane angle. After the beam is properly aligned, i.e. it is in focus, and in the center of field of view, it is still necessary to check if the scanning direction is parallel to the imaging plane. It is possible that the beam is in focus in the center position, but when moved up or down it drifts out of focus due to a tilted scanning

2. DUAL MOUSE-SPIM

angle. This tilt can be compensated by mirror M1, that is placed at the conjugated back focal plane BFP'. Between lenses L3 and L4 a magnified version of the light-sheet will be visible, and the tilt can be checked by placing an alignment target in the optical path while scanning the beam. By tilting mirror M1 up or down, the scanning pattern not only moves up or down, but is also rotated if the mirror surface is not exactly vertical. Since M1 and GM are in conjugated planes, the tilt and offset can be performed independently. The tilt is first fixed by M1 while inspecting the target, and the beam is re-centered by changing the offset on the galvo mirror. Moving the galvo mirror will not introduce tilt, since in this case rotation axis is perpendicular to the reflection plane.

2.4.2 Alignment of detection branches

Since the detection path is equivalent to a wide-field detection scheme, its alignment is much simpler than that of the illumination branches. The only difference is the detection branch merging unit (see Sec. ??.) that features two moving mirrors. This, however doesn't effect the alignment procedure, since the movement direction is parallel to both mirror's surface, meaning that the exact position of the mirrors will not affect the image quality, as long as the mirrors are not clipping the image itself. Stability test were performed to confirm the consistent switching performance of the mirror unit before the final alignment took place (see Sec. ??).

The final alignment procedure

Positioning the tube lens. The position of the tube lens determines the focal plane the is being imaged on the camera sensor. Ideally, the tube lens' distance from the camera sensor is exactly the tube lens focal length, which will ensure the best imaging performance. If the tube lens distance is not correct, the focal plane will be slightly shifted in the axial direction. Although small shifts will not necessarily have detrimental effect on the image quality, because the light sheet can also be shifted accordingly. Because of the shifted focal and image planes, however, the magnification of the system will be affected, and will change depending on the amount of defocus. For this reason we aim for positioning the tube lens as close to the theoretical position as possible.

Our tube lens is a compound, achromatic lens with a center thickness of 12.5 mm, and edge thickness of 11.3 mm. Its effective focal length is 400 mm which will produce a 50x magnified image. Back focal length is 394.33 mm which we measured from the camera chip, and the lens was positioned at this theoretically optimal position.

Adjusting correction collar. The Nikon 25x objectives used for this setup have a built in correction ring that can be used to correct spherical aberrations resulting from refractive index differences when imaging samples behind a coverslip. This can

be also effectively used to correct for any spherical aberrations occurring from imaging through the FEP foil. Although these aberrations are expected to be extremely low, due to the relatively thin, 50 μm foil thickness, and the close matching of refractive index ($n_{FEP} = 1.344$, $n_{H_2O} = 1.333$), for optimal, aberration free image quality it can't be neglected.

The correction collars are adjusted by inspecting a gel suspended fluorescent bead specimen with the microscope, where the beads can act as a reporter of the point spread function of the microscope. The alignment can be performed "live" by inspecting the bead image quality for any aberrations. By gradually changing the correction collar, the ring are minimized on out of focus beads, and the peak intensity is maximized for in focus beads. By moving the correction ring, the focal plane is also slightly shifted, which has to be compensated by shifting the light-sheet correspondingly to coincide with the correct imaging plane.

Adjusting field of view. To allow for proper sampling of the image, we use 50x magnification, which, combined with the 6.5 μm pixel pitch of our sCMOS camera will result in a 0.13 μm pixel size. The full field of view with this magnification is $2048 \times 0.13 = 266.24 \mu\text{m}$. The full field of view the objective provide, are larger than this, at 800 μm . To ensure the best image quality, we align the center of the objective field of view on the camera sensor, since this region has the best optical properties in term of numerical aperture, aberration correction and field flatness.

Field of view alignment can be performed using mirror M4 just before the detection merging unit. To identify the center region of the field of view, diffuse white light is used to illuminate the entire sample chamber, and is imaged on the camera. Then, mirror M4 is adjusted until the top edge of the field of view becomes visible, *i.e.* where the illumination from the chamber is clipped. This will have a circular shape. Then, adjusting the mirror in the orthogonal direction, the left-right position of the field of view can be adjusted, by centering the visible arc on the camera sensor.

After the horizontal direction is centered, vertical centering is performed. This, however can't be centered the same way as the horizontal direction, since for that we would have to misalign the already aligned horizontal position. To determine the center, we move the field of view from the topmost position to the bottom. During this process the number of turns of the adjustment screw is counted (this can be done accurately by using a hex key). After reaching the far end of the field of view, the mirror movement is reversed, and the screw is turned halfway to reach the middle.

2.5 Results

Resolution for Lattice light-sheet [84]: 230 nm in x and 370 nm in z [71]

2. DUAL MOUSE-SPIM

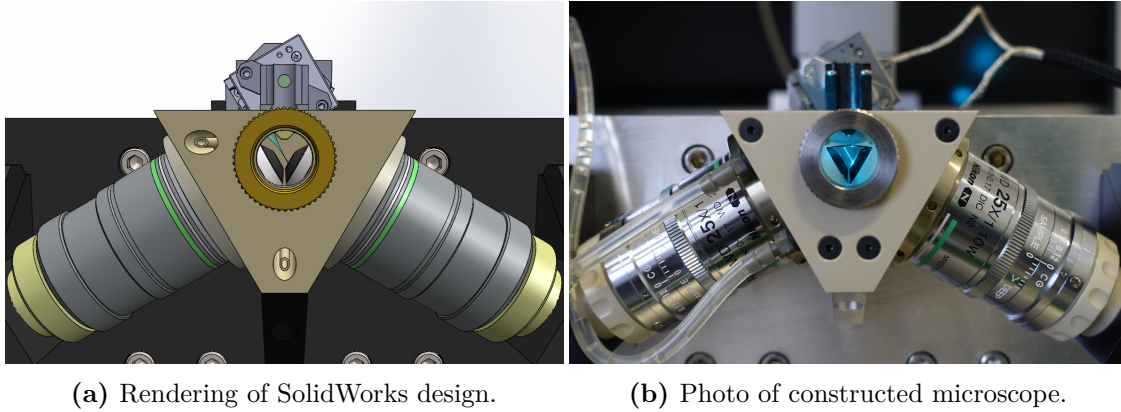


Figure 2.5: Front view of the Dual Mouse-SPIM.

After the design phase, all custom parts were manufactured the the EMBL workshop, and I assembled the microscope on a NewPort X by X optical table (Fig. 2.5).

2.5.1 Characterizing illumination profile

Since a Gaussian beam is used for illumination, it's intensity profile is dependent on the axial position (Eq. 1.17). Although the total intensity at any cross section of the beam is constant, because of the divergent properties, the peak intensity varies. To assess any non-uniformities in the illumination pattern, I measured the illumination beam intensity for each view.

To visualize the beam, the chamber was filled with a fluorescent solution (methylene blue solution in distilled water). In order to increase the signal to noise ratio of these images, a long exposure time of 200 ms were used, and 500 images of each beam was averaged (Fig. 2.6).

2.5.2 Resolution and point spread function measurement

To measure the resolution of the microscope, and characterize its optical performance I performed point spread function measurement using fluorescently labeled beads (TetraSpeck 500 nm, ThermoFisher). The beads were sonicated, and mixed with 0.8% GelRite solution at a final dilution of 1:1000. The gel was loaded in glass capillaries and allowed to cool. After the gel solidified, a ~ 1 mm piece was cut off and placed in the microscope sample holder.

In order to establish an ideal, reference PSF, we simulated the theoretical PSF of the microscope with the Gibson-Lanni model [85], using the MicroscPSF Matlab implementation [86]. The advantage of this model is that it accounts for any differences between the experimental conditions and the design parameters of the objective, and thus it can simulate any possible aberrations that should arise. The adjustable parameters are the

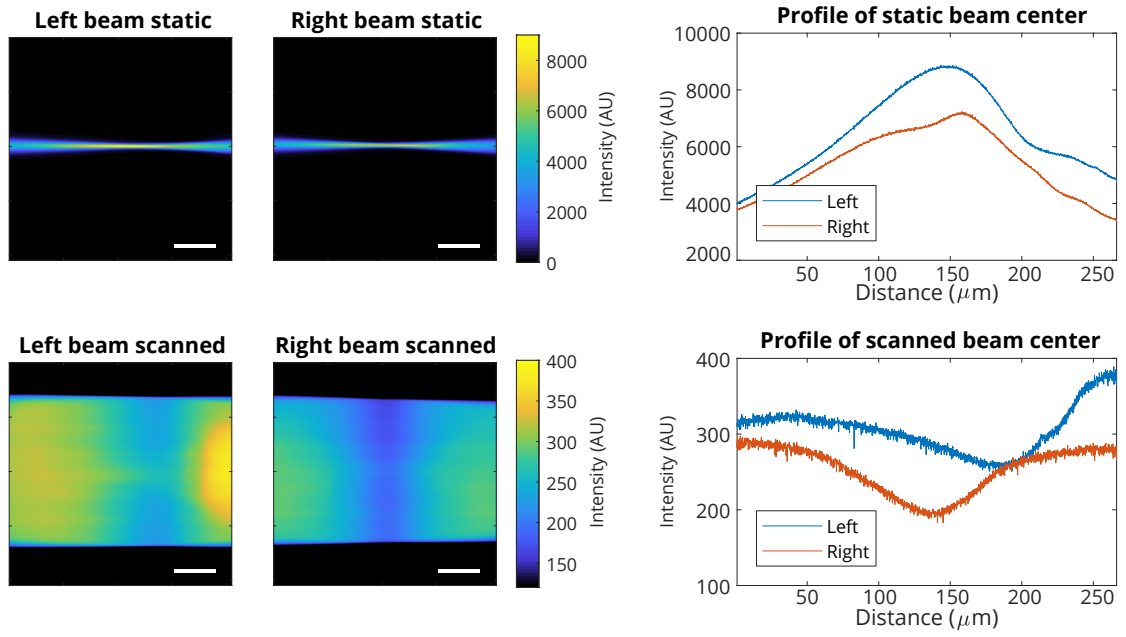


Figure 2.6: Illumination beam profile. Average of 50 stationary beam images for both left and right objectives (top left). Beam intensity profile along the center of each beam is plotted (top right). To simulate scanned beam illumination intensity, each beam image was averaged along the vertical axis (bottom left). Intensity profile of the projections are plotted (bottom right).

following (Fig. ??):

2. DUAL MOUSE-SPIM

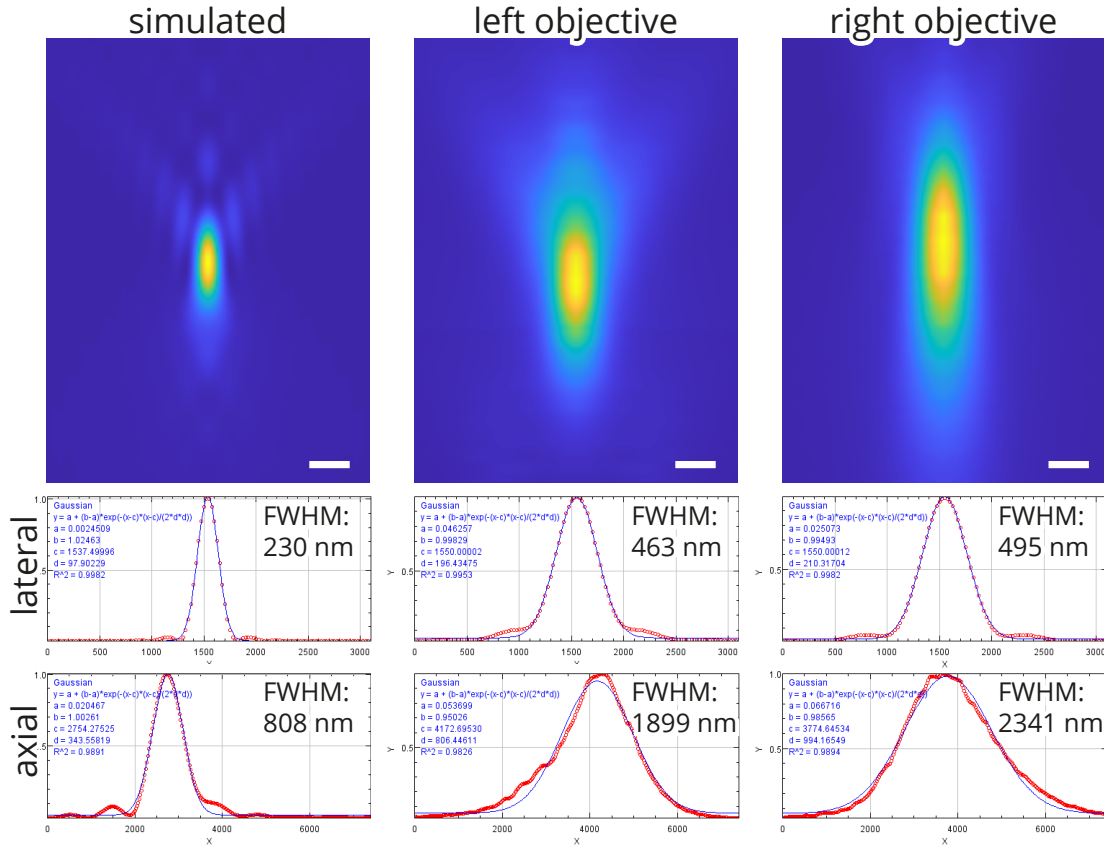


Figure 2.7: Simulated and measured PSF of Dual Mouse-SPIM. Top row: axial sections of simulated and measured point spread functions. Middle row: lateral intensity profile and Gaussian fit. Bottom row: Axial intensity profile and Gaussian fit. Simulations were performed based on the Gibson-Lanni model. Immersion medium and sample refractive index: 1.330, coverslip (FEP foil) refractive index: 1.344, coverslip distance: 1900 μm , coverslip thickness: 50 μm . Scale bar: 500 nm.

Chapter 3

Real-time, GPU accelerated image processing pipeline

3.1 GPU architecture

3.2 Live fusion

3.2.1 MuVi-SPIM

3.2.2 Bead based registration

3.3 B³D image compression

B³D image compression B³D image compression

3.3.1 Data sizes in microscopy

3.3.2 Lossless compression performance

3.3.3 Benchmarking

3.4 Noise dependent lossy compression

3.5 Methods

3. REAL-TIME, GPU ACCELERATED IMAGE PROCESSING PIPELINE

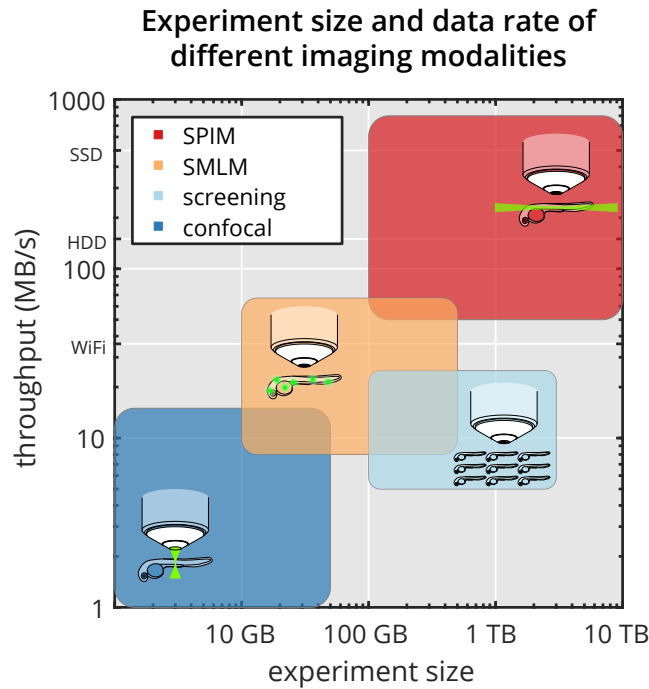


Figure 3.1: Experiment sizes and data rate of different imaging modalities.. Comparison of single-plane illumination microscopy (SPIM, red rectangle), high-content screening (light blue), single molecule localization microscopy (SMLM, orange) and confocal microscopy (blue) by typical experiment size and data production rate (see also Table 3.1).

	imaging device	image size	frame rate	data rate	data size
SPIM	2x sCMOS camera (e.g. Hamamatsu ORCA Flash4.0)	2048x2048	50/s	800 MB/s	10 TB
SMLM	2x EMCCD camera (e.g. Andor iXon Ultra 897)	512x512	56/s	56 MB/s	500 GB
screening	CCD camera (e.g. Hamamatsu ORCA-R2)	1344x1024	8.5s/	22 MB/s	5 TB
confocal	Zeiss LSM 880, 10 channels	512x512	5/s	12.5 MB/s	50 GB

Table 3.1: Data sizes in microscopy. Typical devices used for confocal microscopy, high-content screening, single-molecule localization microscopy and light-sheet microscopy and their data production characteristics. Data visualized on Figure 3.1

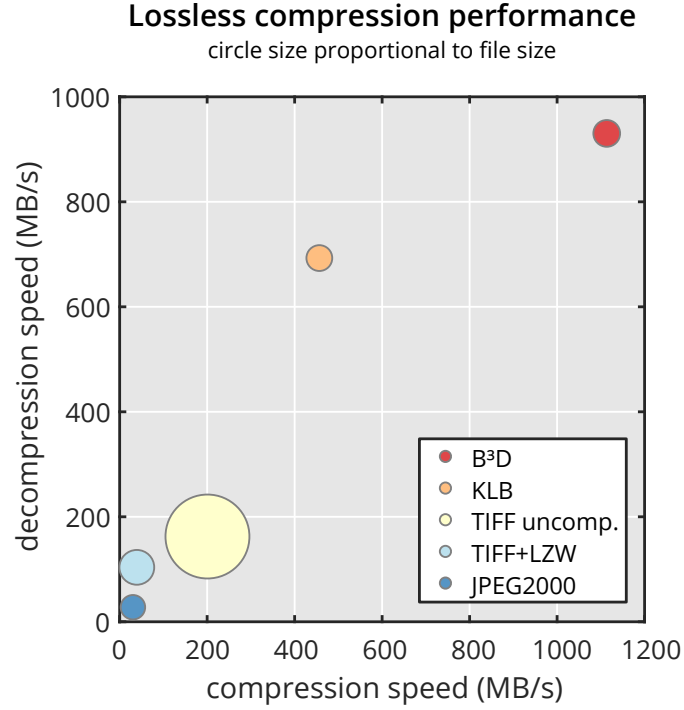


Figure 3.2: Lossless compression performance. Performance comparison of our B³D B³D compression algorithm (red circle) vs. KLB (orange), uncompressed TIFF (light yellow), LZW compressed TIFF (light blue) and JPEG2000 (blue) regarding write speed (horizontal axis), read speed (vertical axis) and file size (circle size). (see also Table 3.2).

	write speed	read speed	CR	file size
B³D	1,115.08 MB/s	928.97 MB/s	9.861	100%
KLB	283.19 MB/s	619.95 MB/s	10.571	93.28%
JPEG2000	31.94 MB/s	26.38 MB/s	11.782	83.69%
JPEG2000	202.32 MB/s	161.08 MB/s	1.00	986.1%
TIFF + LZW	40.85 MB/s	102.37 MB/s	5.822	169.37%

Table 3.2: Lossless compression performance. B³D is compared with various popular lossless image compression methods regarding write speed, read speed and compression ratio (original size / compressed size). Data visualized on Figure 3.2.

3. REAL-TIME, GPU ACCELERATED IMAGE PROCESSING PIPELINE

Dataset name	Imaging modality	Description	Size (MB)
drosophila	SPIM	dataset acquired in MuVi-SPIM of a <i>Drosophila melanogaster</i> embryo expressing H2Av-mCherry nuclear marker	494.53
zebrafish	SPIM	dataset acquired in MuVi-SPIM of a zebrafish embryo expressing b-actin::GCaMP6f calcium sensor	2,408.00
phallusia	SPIM	dataset acquired in MuVi-SPIM of a <i>Phallusia mammillata</i> embryo expressing PH-citrine membrane marker	1,323.88
simulation	SMLM	MT0.N1.LD-2D simulated dataset of microtubules labeled with Alexa Fluor 647 from SMLMS 2016 challenge	156.22
microtubules	SMLM	microtubules immuno-labeled with Alexa Fluor 674-bound antibodies in U2OS cells	1,643.86
lifeact	SMLM	actin network labeled with LifeAct-tdEOS in U2OS cells	3,316.15
dapi	screening	wide field fluorescence images of DAPI stained HeLa Kyoto cells [87]	1,005.38
vsvg	screening	wide field fluorescence images of CFP-tsO45G proteins in HeLa Kyoto cells [87]	1,005.38
membrane	screening	wide field fluorescence images of membrane localized CFP-tsO45G proteins labeled with AlexaFluor647 in HeLa Kyoto cells [87]	1,005.38

Table 3.3: Datasets used for benchmarking compression performance.

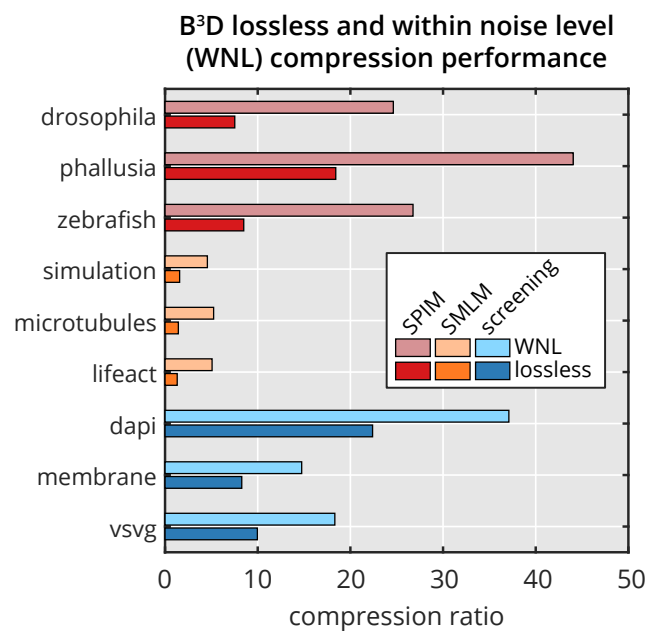


Figure 3.3: Lossless compression performance.. For description of datasets see Table 3.3.

3. REAL-TIME, GPU ACCELERATED IMAGE PROCESSING PIPELINE

Chapter 4

Discussion

4.1 New scientific results

Thesis I. *I have designed and constructed a new light-sheet microscope suitable for high sensitivity imaging of delicate samples. A novel arrangement of two high numerical aperture objectives in 120 degrees allows for near isotropic resolution while increasing light collection efficiency by a factor of two.*

Corresponding publications: [J3],[J1], [J2]

Live imaging of light sensitive specimens, such as a developing mouse embryo is a challenging task

Thesis II. *I have developed a GPU-based image procesing pipeline for multi-view light-sheet microscopy that enables real time fusion of opposing views.*

Corresponding publications: [C1], [C2], [C3]

Thesis III. *I have developed a new image compression algorithm that enables noise dependent lossy compression of light microscopy images, and can reach a compression ratio of 100 fold while preserving the results of downstream data analysis steps.*

Corresponding publications: [J4], [C1], [C2], [C3]

All microscopy images contain inherent noise, that is

Thesis IV. *I have developed a new GPU-based image compression library, B^3D , that implements the algorithm described in Thesis III, and allows for real time compression of microscopy images with a throughput of up to 1 GB/s.*

Corresponding publications: [J4], [C1], [C2], [C3]

B^3D is an efficient, GPU-based image compression library allowing lossless and noise dependent lossy compression of microscopy images. Since many high-speed microscopy

4. DISCUSSION

methods generate immense amounts of data, easily reaching terabytes per experiment, image compression is especially important to efficiently deal with such datasets.

Acknowledgements

ACKNOWLEDGEMENTS

Appendix A

Bill of Materials

Optical components

- Lenses
 - 2×Nikon CFI75 Apo LWD 25x/1.10w water dipping objectives
 - 2×Nikon ITL200 200 mm tube lens
 - 2×200 mm x 25 mm Dia. achromatic lens (Edmunds Optics, #47-645)
 - 2×400 mm x 40 mm Dia. achromatic lens (Edmunds Optics, #49-281)
 - 2×75 mm x 25 mm Dia. achromatic lens (Edmunds Optics, #47-639)
- Filters
 - 2×BrightLine quad-edge dichroic beam splitter (Semrock, Di03-R405/488/561/635-t3-25x36)
 - EdgeBasic 488 nm long pass filter (Semrock, BLP01-488R-25)
 - BrightLine 525/50 band pass filter (Semrock, FF03-525/50-25)
 - EdgeBasic 561 nm long pass filter (Semrock, BLP02-561R-25)
 - RazorEdge 647 nm long pass filter (Semrock, LP02-647RU-25)
- Mirrors
 - 6×1” Broadband Dielectric Elliptical Mirror (Thorlabs, BBE1-E03)
 - 2×30 mm Broadband 1/10 λ Mirror (OptoSigma, TFMS-30C05-4/11)
 - 10 Pack of 1” Protected Silver Mirrors (Thorlabs, PF10-03-P01-10)
 - Knife-Edge Right-Angle Prism Dielectric Mirror (Thorlabs, MRAK25-E02)

Mechanical components

- 40 mm travel range pneumatic cylinder (Airtac, HM-10-040)
- 5/2-way electric valve (Airtac, M-20-510-HN)
- 2×25 mm extended contact bearing steel stage (OptoSigma, TSDH-251C)
- 30x90 mm stainless steel slide (OptoSigma, IPWS-F3090)

APPENDIX A

- close proximity gimbal mirror mount (Thorlabs, GMB1/M)
- 30 mm cage elliptical mirror mount (Thorlabs, KCB1E)

Custom parts

All parts are (anodized) aluminium, unless stated otherwise.

- 2×mirror holder block
- Front plate for objective, chamber and mirror mounting
- Imaging chamber (PEEK)
- Wedge ring and matching threads to fasten objectives
- Camera bridge
- Illumination splitter unit
- adapter plates to mount stages

Electronics

- Embedded system (National Instruments, cRIO-9068) equipped with:
 - 2×C series digital I/O card (NI 9401)
 - 1×C Series 100 kS/s 4-channel Voltage Output Module (NI 9263)
 - 1×C Series 25 kS/s 16-channel Voltage Output Module (NI 9264)
- Omicron SOLE-3 laser combiner, with 488, 561 and 638 nm laser lines
- Andor Zyla 4.2 sCMOS Camera
- Galvanometric scanner mirror (Cambridge Technology, 6210B)
- 6 position filter wheel (Ludl Electronic Products, 96A361)
- Filter wheel controller unit (Ludl Electronic Products, MAC5000)
- 2 piezoelectric stages (Nanos Instruments, LPS-30-30-1-V2_61-S-N)
- 2 stage controller boards (Nanos Instruments, BMC101)

References

The author’s publications

- [J1] P. Strnad, S. Gunther, J. Reichmann, U. Krzic, B. Balazs, G. de Medeiros, N. Norlin, T. Hiiragi, L. Hufnagel, and J. Ellenberg. “Inverted light-sheet microscope for imaging mouse pre-implantation development”. *Nature Methods* 13.2 (Feb. 2016), pp. 139–142. DOI: 10.1038/nmeth.3690 (cit. on pp. 4, 23, 35, 51).
- [J2] P. Hoyer, G. d. Medeiros, B. Balázs, N. Norlin, C. Besir, J. Hanne, H.-G. Kräusslich, J. Engelhardt, S. J. Sahl, S. W. Hell, and L. Hufnagel. “Breaking the diffraction limit of light-sheet fluorescence microscopy by RESOLFT”. *Proceedings of the National Academy of Sciences* 113.13 (Mar. 2016), pp. 3442–3446. DOI: 10.1073/pnas.1522292113 (cit. on pp. 23, 51).
- [J3] G. de Medeiros, B. Balázs, and L. Hufnagel. “Light-sheet imaging of mammalian development”. *Seminars in Cell & Developmental Biology*. Mammalian development 55 (July 2016), pp. 148–155. DOI: 10.1016/j.semcdb.2015.11.001 (cit. on p. 51).
- [J4] B. Balazs, J. Deschamps, M. Albert, J. Ries, and L. Hufnagel. “A real-time compression library for microscopy images”. *bioRxiv* (July 2017), p. 164624. DOI: 10.1101/164624 (cit. on p. 51).

The author’s others publications

- [J5] Z. Jakus, E. Simon, B. Balázs, and A. Mócsai. “Genetic deficiency of Syk protects mice from autoantibody-induced arthritis”. *Arthritis and Rheumatism* 62.7 (July 2010), pp. 1899–1910. DOI: 10.1002/art.27438.
- [J6] B. Györfy, Z. Benke, A. Lánckzy, B. Balázs, Z. Szállási, J. Timár, and R. Schäfer. “RecurrenceOnline: an online analysis tool to determine breast cancer recurrence and hormone receptor status using microarray data”. *Breast Cancer Research and Treatment* (July 2011). DOI: 10.1007/s10549-011-1676-y.

References cited in the thesis

- [J7] W. Shi, B. Balazs, B. Györffy, T. Jiang, W. F. Symmans, C. Hatzis, and L. Pusztai. “Combined analysis of gene expression, DNA copy number, and mutation profiling data to display biological process anomalies in individual breast cancers”. *Breast Cancer Research and Treatment* 144.3 (Mar. 2014), pp. 561–568. DOI: 10.1007/s10549-014-2904-z.

The author’s conference presentations

- [C1] B. Balázs, M. Albert, and L. Hufnagel. “GPU-based image processing for multiview microscopy data”. *Light Sheet Fluorescence Microscopy International Conference*. Sheffield, UK, Sept. 2016 (cit. on p. 51).
- [C2] B. Balázs, M. Albert, and L. Hufnagel. “GPU-based image processing for multi-view microscopy data”. *Focus on Microscopy*. Taipei, Taiwan, Mar. 2016 (cit. on p. 51).
- [C3] B. Balázs, M. Albert, and L. Hufnagel. “GPU-based image processing for multi-view microscopy data”. *Focus on Microscopy*. Bordeaux, France, Apr. 2017 (cit. on p. 51).

References cited in the thesis

- [1] S. F. Gilbert. *Developmental Biology*. 10th. Sinauer Associates, 2013 (cit. on p. 3).
- [2] A. Diaspro. *Optical Fluorescence Microscopy: From the Spectral to the Nano Dimension*. 1st ed. Springer-Verlag Berlin Heidelberg, 2011 (cit. on p. 3).
- [3] Mouse Genome Sequencing Consortium et al. “Initial sequencing and comparative analysis of the mouse genome”. *Nature* 420.6915 (Dec. 2002), pp. 520–562. DOI: 10.1038/nature01262 (cit. on p. 3).
- [4] M. R. Capecchi. “The new mouse genetics: Altering the genome by gene targeting”. *Trends in Genetics* 5 (Jan. 1989), pp. 70–76. DOI: 10.1016/0168-9525(89)90029-2 (cit. on p. 3).
- [5] L. M. Silver. *Mouse Genetics: Concepts and Applications*. Oxford University Press, 1995 (cit. on p. 3).
- [6] R. Hooke. *Micrographia: or Some Physiological Descriptions of Minute Bodies Made by Magnifying Glasses. With Observations and Inquiries Thereupon*. London: J. Martyn and J. Allestry, 1665 (cit. on p. 3).

-
- [7] M. Minsky. “Microscopy apparatus”. US3013467 A. U.S. Classification 356/432, 359/389, 348/79, 250/215; International Classification G02B21/00; Cooperative Classification G02B21/0024, G02B21/002; European Classification G02B21/00M4A, G02B21/00M4. Dec. 1961 (cit. on pp. 3, 12).
- [8] P. Davidovits and M. D. Egger. “Scanning Laser Microscope”. *Nature* 223.5208 (Aug. 1969), pp. 831–831. DOI: 10.1038/223831a0 (cit. on pp. 3, 12).
- [9] P. Davidovits and M. D. Egger. “Photomicrography of Corneal Endothelial Cells in vivo”. *Nature* 244.5415 (Aug. 1973), pp. 366–367. DOI: 10.1038/244366a0 (cit. on p. 3).
- [10] M. D. Garcia, R. S. Udan, A.-K. Hadjantonakis, and M. E. Dickinson. “Live Imaging of Mouse Embryos”. *Cold Spring Harbor Protocols* 2011.4 (Apr. 2011), pdb.top104. DOI: 10.1101/pdb.top104 (cit. on p. 4).
- [11] A. S. Doherty and R. M. Schultz. “Culture of Preimplantation Mouse Embryos”. *Developmental Biology Protocols. Methods in Molecular Biology™*. DOI: 10.1385/1-59259-685-1:47. Humana Press, 2000, pp. 47–52 (cit. on p. 4).
- [12] S. Nowotschin, A. Ferrer-Vaquer, and A.-K. Hadjantonakis. “Chapter 20 - Imaging Mouse Development with Confocal Time-Lapse Microscopy”. *Methods in Enzymology*. Ed. by P. M. W. a. P. M. Soriano. Vol. 476. Guide to Techniques in Mouse Development, Part A: Mice, Embryos, and Cells, 2nd Edition. Academic Press, 2010, pp. 351–377 (cit. on p. 4).
- [13] J. Nichols, B. Zevnik, K. Anastasiadis, H. Niwa, D. Klewe-Nebenius, I. Chambers, H. Schöler, and A. Smith. “Formation of Pluripotent Stem Cells in the Mammalian Embryo Depends on the POU Transcription Factor Oct4”. *Cell* 95.3 (Oct. 1998), pp. 379–391. DOI: 10.1016/S0092-8674(00)81769-9 (cit. on p. 4).
- [14] A. A. Avilion, S. K. Nicolis, L. H. Pevny, L. Perez, N. Vivian, and R. Lovell-Badge. “Multipotent cell lineages in early mouse development depend on SOX2 function”. *Genes & Development* 17.1 (Jan. 2003), pp. 126–140. DOI: 10.1101/gad.224503 (cit. on p. 4).
- [15] C. Costanzi and J. R. Pehrson. “Histone macroH2A1 is concentrated in the inactive X chromosome of female mammals”. *Nature* 393.6685 (June 1998), pp. 599–601. DOI: 10.1038/31275 (cit. on p. 4).
- [16] F. Bard, C. Cannon, R. Barbour, R.-L. Burke, D. Games, H. Grajeda, T. Guido, K. Hu, J. Huang, K. Johnson-Wood, K. Khan, D. Kholodenko, M. Lee, I. Lieberburg, R. Motter, M. Nguyen, F. Soriano, N. Vasquez, K. Weiss, B. Welch, P. Seubert, D. Schenk, and T. Yednock. “Peripherally administered antibodies against amyloid -peptide enter the central nervous system and reduce pathology in a mouse model

References cited in the thesis

- of Alzheimer disease”. *Nature Medicine* 6.8 (Aug. 2000), pp. 916–919. DOI: 10.1038/78682 (cit. on p. 4).
- [17] J.-C. Boisset, W. van Cappellen, C. Andrieu-Soler, N. Galjart, E. Dzierzak, and C. Robin. “In vivo imaging of haematopoietic cells emerging from the mouse aortic endothelium”. *Nature* 464.7285 (Mar. 2010), pp. 116–120. DOI: 10.1038/nature08764 (cit. on p. 4).
- [18] N. Sato, L. Meijer, L. Skaltsounis, P. Greengard, and A. H. Brivanlou. “Maintenance of pluripotency in human and mouse embryonic stem cells through activation of Wnt signaling by a pharmacological GSK-3-specific inhibitor”. *Nature Medicine* 10.1 (Jan. 2004), pp. 55–63. DOI: 10.1038/nm979 (cit. on p. 4).
- [19] S. Falati, P. Gross, G. Merrill-Skoloff, B. C. Furie, and B. Furie. “Real-time in vivo imaging of platelets, tissue factor and fibrin during arterial thrombus formation in the mouse”. *Nature Medicine* 8.10 (Oct. 2002), pp. 1175–1180. DOI: 10.1038/nm782 (cit. on p. 4).
- [20] É. Mezey, K. J. Chandross, G. Harta, R. A. Maki, and S. R. McKercher. “Turning Blood into Brain: Cells Bearing Neuronal Antigens Generated in Vivo from Bone Marrow”. *Science* 290.5497 (Dec. 2000), pp. 1779–1782. DOI: 10.1126/science.290.5497.1779 (cit. on p. 4).
- [21] E. Korotkevich, R. Niwayama, A. Courtois, S. Friesse, N. Berger, F. Buchholz, and T. Hiiragi. “The Apical Domain Is Required and Sufficient for the First Lineage Segregation in the Mouse Embryo”. *Developmental Cell* 40.3 (2017), 235–247.e7. DOI: <http://dx.doi.org/10.1016/j.devcel.2017.01.006> (cit. on p. 4).
- [22] J.-L. Maître, H. Turlier, R. Illukkumbura, B. Eismann, R. Niwayama, F. Nédélec, and T. Hiiragi. “Asymmetric division of contractile domains couples cell positioning and fate specification”. *Nature* 536.7616 (Aug. 2016), pp. 344–348. DOI: 10.1038/nature18958 (cit. on pp. 4, 14).
- [23] J.-E. Dietrich, L. Panavaite, S. Gunther, S. Wennekamp, A. C. Groner, A. Pigge, S. Salvenmoser, D. Trono, L. Hufnagel, and T. Hiiragi. “Venus trap in the mouse embryo reveals distinct molecular dynamics underlying specification of first embryonic lineages”. *EMBO reports* 16.8 (Aug. 2015), pp. 1005–1021. DOI: 10.15252/embr.201540162 (cit. on p. 4).
- [24] J.-L. Maître, R. Niwayama, H. Turlier, F. Nédélec, and T. Hiiragi. “Pulsatile cell-autonomous contractility drives compaction in the mouse embryo”. *Nature Cell Biology* 17.7 (July 2015), pp. 849–855. DOI: 10.1038/ncb3185 (cit. on p. 4).

- [25] P. J. Keller, F. Pampaloni, and E. H. Stelzer. “Life sciences require the third dimension”. *Current Opinion in Cell Biology*. Cell structure and dynamics 18.1 (Feb. 2006), pp. 117–124. DOI: 10.1016/j.ceb.2005.12.012 (cit. on p. 4).
- [26] U. Krzic, S. Gunther, T. E. Saunders, S. J. Streichan, and L. Hufnagel. “Multiview light-sheet microscope for rapid in toto imaging”. *Nature Methods* 9.7 (July 2012). MuVi-SPIM, pp. 730–733. DOI: 10.1038/nmeth.2064 (cit. on pp. 4, 16, 23).
- [27] R. Tomer, K. Khairy, F. Amat, and P. J. Keller. “Quantitative high-speed imaging of entire developing embryos with simultaneous multiview light-sheet microscopy”. *Nature Methods* 9.7 (July 2012). SimView, pp. 755–763. DOI: 10.1038/nmeth.2062 (cit. on pp. 4, 23).
- [28] C. Dunsby. “Optically sectioned imaging by oblique plane microscopy”. *Optics Express* 16.25 (Dec. 2008), pp. 20306–20316. DOI: 10.1364/OE.16.020306 (cit. on p. 4).
- [29] J. Capoulade, M. Wachsmuth, L. Hufnagel, and M. Knop. “Quantitative fluorescence imaging of protein diffusion and interaction in living cells”. *Nature Biotechnology* 29.9 (Sept. 2011), pp. 835–839. DOI: 10.1038/nbt.1928 (cit. on p. 5).
- [30] J. W. Lichtman and J.-A. Conchello. “Fluorescence microscopy”. *Nature Methods* 2.12 (Dec. 2005), pp. 910–919. DOI: 10.1038/nmeth817 (cit. on p. 5).
- [31] *Spectra Viewer*. Text (cit. on p. 5).
- [32] O. Shimomura, F. H. Johnson, and Y. Saiga. “Extraction, purification and properties of aequorin, a bioluminescent protein from the luminous hydromedusan, *Aequorea*”. *Journal of Cellular and Comparative Physiology* 59 (June 1962). first purification of GFP from jellyfish, pp. 223–239 (cit. on p. 6).
- [33] D. C. Prasher, V. K. Eckenrode, W. W. Ward, F. G. Prendergast, and M. J. Cormier. “Primary structure of the *Aequorea victoria* green-fluorescent protein”. *Gene* 111.2 (Feb. 1992). cloning GFP cDNA, pp. 229–233. DOI: 10.1016/0378-1119(92)90691-H (cit. on p. 6).
- [34] M. Chalfie, Y. Tu, G. Euskirchen, W. W. Ward, and D. C. Prasher. “Green fluorescent protein as a marker for gene expression”. *Science* 263.5148 (Feb. 1994). GFP in *c. elegans* / nematodes, pp. 802–805. DOI: 10.1126/science.8303295 (cit. on p. 6).
- [35] A. Amsterdam, S. Lin, and N. Hopkins. “The *Aequorea victoria* Green Fluorescent Protein Can Be Used as a Reporter in Live Zebrafish Embryos”. *Developmental Biology* 171.1 (Sept. 1995). first GFP zebrafish, pp. 123–129. DOI: 10.1006/dbio.1995.1265 (cit. on p. 6).

References cited in the thesis

- [36] M. Okabe, M. Ikawa, K. Kominami, T. Nakanishi, and Y. Nishimune. “‘Green mice’ as a source of ubiquitous green cells”. *FEBS Letters* 407.3 (May 1997). first EGFP mouse, pp. 313–319. DOI: 10.1016/S0014-5793(97)00313-X (cit. on p. 6).
- [37] R. Heim, D. C. Prasher, and R. Y. Tsien. “Wavelength mutations and posttranslational autooxidation of green fluorescent protein.” *Proceedings of the National Academy of Sciences of the United States of America* 91.26 (Dec. 1994), pp. 12501–12504 (cit. on p. 6).
- [38] R. Heim and R. Y. Tsien. “Engineering green fluorescent protein for improved brightness, longer wavelengths and fluorescence resonance energy transfer”. *Current Biology* 6.2 (Feb. 1996), pp. 178–182. DOI: 10.1016/S0960-9822(02)00450-5 (cit. on p. 6).
- [39] B. P. Cormack, R. H. Valdivia, and S. Falkow. “FACS-optimized mutants of the green fluorescent protein (GFP)”. *Gene. Fluorescent Proteins and Applications* 173.1 (1996), pp. 33–38. DOI: 10.1016/0378-1119(95)00685-0 (cit. on p. 6).
- [40] R. F. Service. “Three Scientists Bask in Prize’s Fluorescent Glow”. *Science* 322.5900 (Oct. 2008), pp. 361–361. DOI: 10.1126/science.322.5900.361 (cit. on p. 6).
- [41] E. Abbe. “Beiträge zur Theorie des Mikroskops und der mikroskopischen Wahrnehmung”. *Archiv für mikroskopische Anatomie* 9.1 (1873), pp. 413–418. DOI: 10.1007/BF02956173 (cit. on p. 8).
- [42] M. Born and E. Wolf. *Principles of Optics: Electromagnetic Theory of Propagation, Interference and Diffraction of Light*. Elsevier, June 2013 (cit. on p. 8).
- [43] C. J. R. Sheppard and H. J. Matthews. “Imaging in high-aperture optical systems”. *JOSA A* 4.8 (Aug. 1987), pp. 1354–1360. DOI: 10.1364/JOSAA.4.001354 (cit. on p. 8).
- [44] J. Swoger, J. Huisken, and E. H. K. Stelzer. “Multiple imaging axis microscopy improves resolution for thick-sample applications”. *Optics Letters* 28.18 (Sept. 2003), p. 1654. DOI: 10.1364/OL.28.001654 (cit. on pp. 12, 22).
- [45] J. Swoger, P. Verveer, K. Greger, J. Huisken, and E. H. K. Stelzer. “Multi-view image fusion improves resolution in three-dimensional microscopy”. *Optics Express* 15.13 (2007), p. 8029. DOI: 10.1364/OE.15.008029 (cit. on p. 12).
- [46] E. H. Stelzer and S. Lindek. “Fundamental reduction of the observation volume in far-field light microscopy by detection orthogonal to the illumination axis: confocal theta microscopy”. *Optics Communications* 111.5–6 (Oct. 1994), pp. 536–547. DOI: 10.1016/0030-4018(94)90533-9 (cit. on p. 14).

-
- [47] S. Aldaz, L. M. Escudero, and M. Freeman. “Live Imaging of *Drosophila* Imaginal Disc Development”. *Proceedings of the National Academy of Sciences* 107.32 (Aug. 2010), pp. 14217–14222. DOI: 10.1073/pnas.1008623107 (cit. on p. 14).
 - [48] E. G. Reynaud, U. Kržič, K. Greger, and E. H. Stelzer. “Light sheet-based fluorescence microscopy: more dimensions, more photons, and less photodamage”. *HFSP Journal* 2.5 (Oct. 2008), pp. 266–275. DOI: 10.2976/1.2974980 (cit. on pp. 14, 16).
 - [49] Stelzer. “Contrast, resolution, pixelation, dynamic range and signal-to-noise ratio: fundamental limits to resolution in fluorescence light microscopy”. *Journal of Microscopy* 189.1 (Jan. 1998). This is also the reason why it is sufficient to store the square root of the count rate. That number will contain all the available information., pp. 15–24. DOI: 10.1046/j.1365-2818.1998.00290.x (cit. on p. 15).
 - [50] H. Siedentopf and R. Zsigmondy. “Über Sichtbarmachung und Größenbestimmung ultramikroskopischer Teilchen, mit besonderer Anwendung auf Goldrubingläser”. *Annalen der Physik* 315.1 (1902), pp. 1–39. DOI: 10.1002/andp.19023150102 (cit. on p. 15).
 - [51] A. H. Voie, D. H. Burns, and F. A. Spelman. “Orthogonal-plane fluorescence optical sectioning: three-dimensional imaging of macroscopic biological specimens”. *Journal of Microscopy* 170.Pt 3 (June 1993), pp. 229–36. DOI: 8371260 (cit. on p. 16).
 - [52] A. H. Voie and F. A. Spelman. “Three-dimensional reconstruction of the cochlea from two-dimensional images of optical sections”. *Computerized Medical Imaging and Graphics* 19.5 (Sept. 1995), pp. 377–384. DOI: 10.1016/0895-6111(95)00034-8 (cit. on p. 16).
 - [53] D. Huber, M. Keller, and D. Robert. “3D light scanning macrography”. *Journal of Microscopy* 203.2 (Aug. 2001), pp. 208–213. DOI: 10.1046/j.1365-2818.2001.00892.x (cit. on p. 16).
 - [54] E. Fuchs, J. S. Jaffe, R. A. Long, and F. Azam. “Thin laser light sheet microscope for microbial oceanography”. *Optics Express* 10.2 (Jan. 2002), pp. 145–154. DOI: 10.1364/OE.10.000145 (cit. on p. 16).
 - [55] J. Huiskens, J. Swoger, F. Del Bene, J. Wittbrodt, and E. H. K. Stelzer. “Optical Sectioning Deep Inside Live Embryos by Selective Plane Illumination Microscopy”. *Science* 305.5686 (2004), pp. 1007–1009 (cit. on pp. 16, 23).
 - [56] J. Huiskens and D. Y. R. Stainier. “Selective plane illumination microscopy techniques in developmental biology”. *Development* 136.12 (June 2009), pp. 1963–1975. DOI: 10.1242/dev.022426 (cit. on p. 16).

References cited in the thesis

- [57] M. Weber and J. Huiskens. “Light sheet microscopy for real-time developmental biology”. *Current Opinion in Genetics & Development* 21.5 (2011), pp. 566–572. DOI: 10.1016/j.gde.2011.09.009 (cit. on p. 16).
- [58] P. J. Keller, A. D. Schmidt, J. Wittbrodt, and E. H. K. Stelzer. “Reconstruction of Zebrafish Early Embryonic Development by Scanned Light Sheet Microscopy”. *Science* 322.5904 (Nov. 2008), pp. 1065–1069. DOI: 10.1126/science.1162493 (cit. on pp. 16, 20).
- [59] A. Kaufmann, M. Mickoleit, M. Weber, and J. Huiskens. “Multilayer mounting enables long-term imaging of zebrafish development in a light sheet microscope”. *Development* 139.17 (Sept. 2012). mounting methods, FEP, pp. 3242–3247. DOI: 10.1242/dev.082586 (cit. on p. 16).
- [60] M. Mickoleit, B. Schmid, M. Weber, F. O. Fahrbach, S. Hombach, S. Reischauer, and J. Huiskens. “High-resolution reconstruction of the beating zebrafish heart”. *Nature Methods* 11.9 (Sept. 2014), pp. 919–922. DOI: 10.1038/nmeth.3037 (cit. on p. 16).
- [61] H.-U. Dodt, U. Leischner, A. Schierloh, N. Jährling, C. P. Mauch, K. Deininger, J. M. Deussing, M. Eder, W. Zieglgänsberger, and K. Becker. “Ultramicroscopy: three-dimensional visualization of neuronal networks in the whole mouse brain”. *Nature Methods* 4.4 (Mar. 2007), pp. 331–336. DOI: 10.1038/nmeth1036 (cit. on p. 16).
- [62] F. Cella Zanacchi, Z. Lavagnino, M. Perrone Donnorso, A. Del Bue, L. Furia, M. Faretta, and A. Diaspro. “Live-cell 3D super-resolution imaging in thick biological samples”. *Nature Methods* 8.12 (Dec. 2011), pp. 1047–1049. DOI: 10.1038/nmeth.1744 (cit. on p. 16).
- [63] K. Greger, J. Swoger, and E. H. K. Stelzer. “Basic building units and properties of a fluorescence single plane illumination microscope”. *Review of Scientific Instruments* 78.2 (Feb. 2007), pp. 023705–023705–7. DOI: doi:10.1063/1.2428277 (cit. on p. 19).
- [64] U. Kržič. “Multiple-view microscopy with light-sheet based fluorescence microscope”. PhD thesis. Germany: Ruperto-Carola University of Heidelberg, 2009 (cit. on pp. 19, 24).
- [65] B. E. A. Saleh and M. C. Teich. *Fundamentals of Photonics*. John Wiley & Sons, Mar. 2007 (cit. on p. 19).
- [66] J. Huiskens, J. Swoger, and E. H. K. Stelzer. “Three-dimensional optical manipulation using four collimated intersecting laser beams”. *Optics Express* 15.8 (Apr. 2007), pp. 4921–4928. DOI: 10.1364/OE.15.004921 (cit. on p. 23).

- [67] Y. Wu, A. Ghitani, R. Christensen, A. Santella, Z. Du, G. Rondeau, Z. Bao, D. Colón-Ramos, and H. Shroff. “Inverted selective plane illumination microscopy (iSPIM) enables coupled cell identity lineaging and neurodevelopmental imaging in *Caenorhabditis elegans*”. *Proceedings of the National Academy of Sciences* 108.43 (Oct. 2011). iSPIM, tracking *C. elegans* nuclei, pp. 17708–17713. DOI: 10.1073/pnas.1108494108 (cit. on p. 23).
- [68] A. Kumar, Y. Wu, R. Christensen, P. Chandris, W. Gandler, E. McCreedy, A. Bokinsky, D. A. Colón-Ramos, Z. Bao, M. McAuliffe, G. Rondeau, and H. Shroff. “Dual-view plane illumination microscopy for rapid and spatially isotropic imaging”. *Nature Protocols* 9.11 (Nov. 2014). diSPIM, pp. 2555–2573. DOI: 10.1038/nprot.2014.172 (cit. on p. 23).
- [69] J. Huiskens and D. Y. R. Stainier. “Even fluorescence excitation by multidirectional selective plane illumination microscopy (mSPIM)”. *Optics Letters* 32.17 (2007), pp. 2608–2610. DOI: 10.1364/OL.32.002608 (cit. on p. 23).
- [70] B. Schmid, G. Shah, N. Scherf, M. Weber, K. Thierbach, C. P. Campos, I. Roeder, P. Aanstad, and J. Huiskens. “High-speed panoramic light-sheet microscopy reveals global endodermal cell dynamics”. *Nature Communications* 4 (July 2013). zebrafish sphere projection + FEP tube. DOI: 10.1038/ncomms3207 (cit. on p. 23).
- [71] R. K. Chhetri, F. Amat, Y. Wan, B. Höckendorf, W. C. Lemon, and P. J. Keller. “Whole-animal functional and developmental imaging with isotropic spatial resolution”. *Nature Methods* 12.12 (Dec. 2015), pp. 1171–1178. DOI: 10.1038/nmeth.3632 (cit. on pp. 23, 41).
- [72] M. Temerinac-Ott, O. Ronneberger, P. Ochs, W. Driever, T. Brox, and H. Burkhardt. “Multiview Deblurring for 3-D Images from Light-Sheet-Based Fluorescence Microscopy”. *IEEE Transactions on Image Processing* 21.4 (Apr. 2012), pp. 1863–1873. DOI: 10.1109/TIP.2011.2181528 (cit. on p. 24).
- [73] M. Temerinac-Ott, O. Ronneberger, R. Nitschke, W. Driever, and H. Burkhardt. “Spatially-variant Lucy-Richardson deconvolution for multiview fusion of microscopical 3D images”. *2011 IEEE International Symposium on Biomedical Imaging: From Nano to Macro*. Mar. 2011, pp. 899–904. DOI: 10.1109/ISBI.2011.5872549 (cit. on p. 24).
- [74] K. Sayood. *Introduction to Data Compression, Fourth Edition*. 4th ed. The Morgan Kaufmann Series in Multimedia Information and Systems. Morgan Kaufmann, 2012 (cit. on p. 25).
- [75] C. E. Shannon. “A mathematical theory of communication”. *The Bell System Technical Journal* 27.4 (Oct. 1948), pp. 623–656. DOI: 10.1002/j.1538-7305.1948.tb00917.x (cit. on p. 25).

References cited in the thesis

- [76] C. E. Shannon. “A mathematical theory of communication”. *The Bell System Technical Journal* 27.3 (July 1948), pp. 379–423. DOI: 10.1002/j.1538-7305.1948.tb01338.x (cit. on p. 25).
- [77] D. A. Huffman. “A Method for the Construction of Minimum-Redundancy Codes”. *Proceedings of the IRE* 40.9 (Sept. 1952), pp. 1098–1101. DOI: 10.1109/JRPROC.1952.273898 (cit. on p. 26).
- [78] N. Ahmed, T. Natarajan, and K. R. Rao. “Discrete Cosine Transform”. *IEEE Transactions on Computers* C-23.1 (Jan. 1974), pp. 90–93. DOI: 10.1109/T-C.1974.223784 (cit. on p. 30).
- [79] G. Mallat. “A theory for multiresolution signal decomposition : the wavelet representation”. *IEEE Transaction on Pattern Analysis and Machine Intelligence* (1989) (cit. on p. 32).
- [80] W. B. Pennebaker and J. L. Mitchell. *JPEG: Still Image Data Compression Standard*. Springer Science & Business Media, Dec. 1992 (cit. on p. 34).
- [81] M. Weinberger, G. Seroussi, and G. Sapiro. “The LOCO-I lossless image compression algorithm: principles and standardization into JPEG-LS”. *IEEE Transactions on Image Processing* 9.8 (Aug. 2000), pp. 1309–1324. DOI: 10.1109/83.855427 (cit. on p. 34).
- [82] G. Donnert, C. Eggeling, and S. W. Hell. “Major signal increase in fluorescence microscopy through dark-state relaxation”. *Nature Methods* 4.1 (Jan. 2007). peak intensity more important than average, pp. 81–86. DOI: 10.1038/nmeth986 (cit. on p. 35).
- [83] N. Ji, J. C. Magee, and E. Betzig. “High-speed, low-photodamage nonlinear imaging using passive pulse splitters”. *Nature Methods* 5.2 (Feb. 2008). TPE, pulse splitter, peak intensity more important than average, pp. 197–202. DOI: 10.1038/nmeth.1175 (cit. on p. 35).
- [84] B.-C. Chen, W. R. Legant, K. Wang, L. Shao, D. E. Milkie, M. W. Davidson, C. Janetopoulos, X. S. Wu, J. A. Hammer, Z. Liu, B. P. English, Y. Mimori-Kiyosue, D. P. Romero, A. T. Ritter, J. Lippincott-Schwartz, L. Fritz-Laylin, R. D. Mullins, D. M. Mitchell, J. N. Bembenek, A.-C. Reymann, R. Böhme, S. W. Grill, J. T. Wang, G. Seydoux, U. S. Tulu, D. P. Kiehart, and E. Betzig. “Lattice light-sheet microscopy: Imaging molecules to embryos at high spatiotemporal resolution”. *Science* 346.6208 (Oct. 2014), p. 1257998. DOI: 10.1126/science.1257998 (cit. on p. 41).

-
- [85] S. F. Gibson and F. Lanni. “Experimental test of an analytical model of aberration in an oil-immersion objective lens used in three-dimensional light microscopy”. *JOSA A* 9.1 (Jan. 1992), pp. 154–166. DOI: 10.1364/JOSAA.9.000154 (cit. on p. 42).
- [86] J. Li, F. Xue, and T. Blu. “Fast and accurate three-dimensional point spread function computation for fluorescence microscopy”. *JOSA A* 34.6 (June 2017), pp. 1029–1034. DOI: 10.1364/JOSAA.34.001029 (cit. on p. 42).
- [87] J. C. Simpson, B. Joggerst, V. Laketa, F. Verissimo, C. Cetin, H. Erfle, M. G. Bexiga, V. R. Singan, J.-K. Hériché, B. Neumann, A. Mateos, J. Blake, S. Bechtel, V. Benes, S. Wiemann, J. Ellenberg, and R. Pepperkok. “Genome-wide RNAi screening identifies human proteins with a regulatory function in the early secretory pathway”. *Nature Cell Biology* 14.7 (July 2012), pp. 764–774. DOI: 10.1038/ncb2510 (cit. on p. 48).